Temperature response during rapid depressurization of CO_2 in a pipe: Experiments and fluid-dynamics modelling

Alexandra Metallinou Log*, Morten Hammer, Han Deng, Anders Austegard, Svend Tollak Munkejord

SINTEF Energy Research, P.O. Box 4761 Torgarden, NO-7465 Trondheim, Norway

Abstract

The temperature evolution of CO_2 during full-bore pipe depressurization events is relevant for risk assessment, e.g., for CO_2 transport in the context of CO_2 capture and storage (CCS). We analyse and model the temperature evolution for four different initial temperatures between $T_0 = 4.6\,°C$ and $T_0 = 40\,°C$ at supercritical pressures. All the experiments showed an analogous temperature evolution, reaching similar minimum temperatures along the pipe. The warmer the initial temperature, the earlier dry-out and faster temperature recovery was observed. Also, the coldest experiment showed evidence of formation of more dry ice.

We employ the homogeneous equilibrium model (HEM) with different heat-transfer correlations and a two-fluid model (TFM) with different slip models in order to understand the observed data. The results indicate that the heat transfer changes significantly with different thermodynamic states for the CO_2. Also, the HEM and the TFM with a RELAP-type friction model performed reasonably well at the outlet and at the closed end of the pipe, but none of the tested models were able to fully describe the strong spatial and temporal gradients observed along the pipe during the depressurization.

Keywords: carbon dioxide, decompression, dense phase, heat transfer, two-fluid model, dry ice

1. Introduction

CO_2 capture and storage (CCS) is considered one of the essential technologies to mitigate climate change (Shukla *et al.*, 2022). For CCS to reach the scale needed for significant impact, deployment must be scaled up to capture and store several gigatonnes of CO_2 annually by 2050 (IEA, 2020). Capture plants and storage sites will in general be separated, and a large-scale transport infrastructure will be required (Moe *et al.*, 2020), including ships (Roussanaly *et al.*, 2021), pipelines (Aursand *et al.*, 2013) and other means. To design and operate CO_2 transportation and injection systems safely and efficiently, validated flow models for single- and multiphase CO_2 and CO_2-rich mixtures are needed (Munkejord *et al.*, 2016; Vitali *et al.*, 2022).

Indeed, the operational window of CO_2 pipelines will often be between the critical point (31.0 °C, 73.8 bar), above which there are no distinct gas or liquid phases, and the triple point (–56.6 °C, 5.17 bar), at which vapour, liquid and solid exist in equilibrium. Therefore, for many relevant operational scenarios, such as start-up, shut-down and depressurization, phase transitions can occur and there is a strong coupling between pressure and temperature. This means that one cannot calculate the one without the other. In particular, both pressure and temperature must be accurately modelled if key phenomena such as dry-out of the liquid phase or dry-ice formation are to be predicted. Furthermore, depressurization of a pipeline will lead to low temperatures, and it is of interest to avoid both metallic

*Corresponding author.
Email address: alexandra.log@sintef.no (Alexandra Metallinou Log)

and non-metallic materials becoming brittle or otherwise have their function impaired (Munkejord *et al.*, 2013). Predicting the temperature evolution is therefore of high importance.

In the majority of previous studies on CO_2 pipe depressurization, the rapid pressure response has been the main interest. This is due to its key role in understanding running ductile fracture (RDF) in a pipeline. In an RDF, a defect in the pipeline develops into a fracture running along the pipeline, sustained by the pressure forces exerted by the escaping fluid (see e.g., Maxey, 1974; Skarsvåg *et al.*, 2023).

In studies aimed at analysing pressure-propagation waves, heat transfer modelling is often ignored because its effect is small for short time-frames (Brown *et al.*, 2013; Elshahomi *et al.*, 2015; Aursand *et al.*, 2016; Liu *et al.*, 2018; Flechas *et al.*, 2020; Xiao *et al.*, 2020). However, for longer time-frames (on the scale of seconds and longer), the heat transfer between the fluid and the pipe wall is highly relevant, and strongly affects the phase behaviour in the pipe (see e.g., Munkejord and Hammer, 2015). Munkejord and Hammer (2015) showed that it is necessary to solve the transient heat-transfer equation in the pipe wall to obtain accurate temperature predictions for full pipe depressurization tests. It is then necessary to estimate the fluid-to-wall heat-transfer coefficient.

Many transient CO_2 flow models that include heat transfer through the pipe wall apply a heat-transfer correlation which only accounts for forced convection, even when phase change occurs in the flow (Brown *et al.*, 2014; Drescher *et al.*, 2014; Samuel and Mahgerefteh, 2019; Sacconi and Mahgerefteh, 2020; Bhuvankar *et al.*, 2023). When only forced convection is included, the Dittus and Boelter (1930) or Colburn (see Bejan, 1993, Chap. 6) correlations are usually applied. Munkejord and Hammer (2015) found some improvement in the temperature prediction of their flow model by accounting for saturated flow boiling using the Gungor and Winterton (1987) heat transfer correlation, based on data from Drescher *et al.* (2014) for decompression from the dense phase. However, Munkejord *et al.* (2016) tested the model against depressurization data from the CO2pipetrans project[1], and found that ignoring boiling enhancement seemed to perform better. Clausen *et al.* (2012) reported pressure and temperature data for the depressurization of a 50 km long pipeline along with modelling results employing a commercially available pipeline simulator. For the temperature, only moderate agreement between simulations and measurements was observed. Because the pipeline was only instrumented at the outlets, and because of some uncertainty regarding the initial conditions, clear conclusions regarding the reason for the disagreement could not be reached.

Zheng *et al.* (2017) and Martynov *et al.* (2018) studied the temperature evolution, and particularly solid formation, during CO_2 pipe depressurization. They assumed that for liquid–gas two-phase flow, heat transfer from nucleate boiling would dominate, and applied the Rohsenow (Collier and Thome, 1994, Sec. 4.4.3) heat-transfer correlation for this condition. Their model fitted the pressure data well, but the predicted temperature deviated from measurements after solid formation and could not capture the liquid dry-out point for one of their validation tests against experimental data. More recently, Bhuvankar *et al.* (2023) obtained a better prediction of the dry-out temperature for pipe depressurization Test 6 of Munkejord *et al.* (2020a) when only convective heat transfer was considered, as opposed to Munkejord *et al.* (2020a) who applied the Gungor and Winterton correlation.

Based on the literature cited above, it is not clear how to best model heat transfer during depressurization of a CO_2 pipe. Furthermore, most of the above studies applied the homogeneous equilibrium flow model (HEM), in which the phases are assumed to have the same pressure, temperature, chemical potential and velocity. Munkejord *et al.* (2020a) suggested that better temperature approximations could be achieved if the two-fluid model (TFM) is applied instead, as it allows the liquid and gas phases to flow at different velocities. The present study therefore aims to fill the knowledge gap by testing several different heat-transfer correlations for the HEM, and comparing the temperature predictions of the HEM and the TFM, to assess the effect of allowing slip between the phases.

As the pressure response has been the main focus in most depressurization studies, there is also much less temperature data than pressure data available for model validation. Recently, some

[1]These data were previously openly available at `https://www.dnvgl.com/oilgas/innovation-development/joint-industry-projects/co2pipetrans.html`, but the authors could no longer find the data using this link at the time of writing.

experimental campaigns have been conducted for the explicit study of the temperature evolution during CO_2 pipe depressurization. Cao *et al.* (2018) conducted a series of pipe depressurization tests for pure CO_2 from both the gaseous and dense phase through orifices, including a full bore release. The pipe was 257 m long, and a total of 14 temperature sensors were placed at the top, bottom and side of the pipe at various locations along the pipe. Cao *et al.* (2020) designed a new type of thermocouple which provided temperature measurements at six vertical positions across the pipe. These thermocouples were placed at six positions along the pipe, providing a total of 36 temperature data sources. This detailed data was presented for a dense-phase CO_2 release through a 50 mm orifice. The data provided an indication of the phase distribution in the pipe during the decompression. Yu *et al.* (2024b) employed these data to build a vessel blowdown model for large-scale pipelines with small-diameter leaks of pure CO_2. Yu *et al.* (2024a) also conducted new pipe depressurization experiments with CO_2-N_2 mixtures, focused on puncture releases. In these experiments, temperature measurements were made at six locations along the 258 m long pipe. At each location, five thermocouples were grouped to measure the vertical temperature distribution during the release.

In the present study we consider full-bore releases, focusing on a series of CO_2 pipe depressurization experiments from the dense phase with different initial temperatures that was conducted at the ECCSEL pipe depressurization facility (ECCSEL, 2021). The facility has thermocouples at 15 locations along a 61 m long pipe. At four of these locations the temperature is measured at the top, bottom and side of the pipe. Though the initial rapid pressure response has been analysed and modelled (Munkejord *et al.*, 2020a, 2021; Hammer *et al.*, 2022; Log *et al.*, 2024a,b), the temperature measurements have not yet been studied in detail. They provide excellent input for flow model validation.

The purpose of this work is two-fold, focusing both on the analysis of experimental temperature measurements, and on the assessment of flow and heat-transfer models. We present the temperature data for four full-bore CO_2 depressurization tests with initial temperatures in the range 5 °C to 40 °C. The tests provide valuable insight on how the temperature evolution, dry-out and solid formation in the pipe during depressurization vary with different initial conditions. The data are analysed, and then employed in an assessment of the HEM and the TFM, including various heat-transfer correlations for boiling flows applied with the HEM.

The remainder of the article is structured as follows. In Section 2, the experiments are briefly presented. In Section 3 the governing equations of the HEM and TFM are provided, the heat-transfer calculations are described, and the numerical solution method is outlined. Next, the experimental results are discussed and analysed in Section 4.1, and the performance of the flow models and heat-transfer correlations in predicting the temperature evolution in the pipe are assessed in Section 4.2. Finally, the results are summarized and concluding remarks are provided in Section 5.

2. Experiments

In this section, the experimental facility and experiment procedure is summarized, and the experiments studied in this work are introduced.

2.1. ECCSEL depressurization facility and test procedure

The ECCSEL depressurization facility has been described in previous publications. See Munkejord *et al.* (2020a) for a more detailed description. A brief overview is provided here for completeness.

The ECCSEL depressurization facility (ECCSEL, 2021) has a test section consisting of a 61.67 m pipe made of 316L stainless steel, and it is insulated with a 60 mm thick layer of glass wool. The thermal properties of these materials are reported in Table 1. The inner diameter of the pipe is 40.8 mm and the outer diameter is 48.3 mm, and the mean roughness, R_a, of the inner surface of the pipe is 0.2 µm–0.3 µm. Figure 1 shows a schematic overview of the pipe. A rupture disk with a disk holder is installed at the pipe outlet. The specified burst pressure of the disk is 120 barg±5% at 22 °C.

The experimental procedure is as follows. First, the rupture disk is installed and the system is evacuated. Then the test section is filled with CO_2 and pressurized. When the pressure reaches about

Table 1: Density and thermal properties of the pipe metal and insulation.

	Radial segment (mm)	Density ($kg\,m^{-3}$)	Thermal conductivity ($W\,m^{-1}\,K^{-1}$)	Specific heat ($J\,kg^{-1}\,K^{-1}$)
Pipe steel	20.4–24.15	8000	15	500
Insulation	24.15–84.15	75	0.032	840

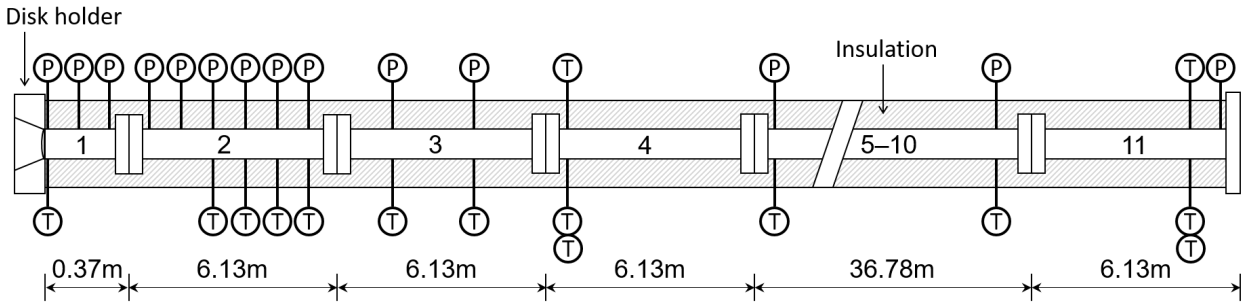

Figure 1: Test section (dimensions are not to scale; pipe nos. 5–10 and corresponding sensors are omitted.)

70% of the desired value, the fluid is circulated to achieve a uniform temperature along the test section. This pressure level for circulation is chosen to ensure that the rupture disk will not break before a uniform temperature is reached in the pipe, while being safely away from the lower pressure two-phase region. The fluid temperature is controlled using heating elements wrapped around the test section. The pressure is then increased gradually by alternating filling and circulation of CO_2 until the disk ruptures. The valves used for filling and circulation of the fluid are automatically closed once the rapid pressure drop is detected, and the heating cables are turned off.

2.2. Instrumentation

Along the pipe, 16 fast-response pressure transducers of the type Kulite CTL-190(M) are flush-mounted to the inner surface to capture the pressure transients during depressurization. 23 Type E thermocouples are installed to measure the temperature changes. 15 of the thermocouples are placed at axial positions along the pipe. At four locations there are also thermocouples mounted at the top and bottom of the pipe to capture any flow stratification. The uncertainty of the temperature measurements has been estimated to be around ±0.22 °C (Munkejord *et al.*, 2020a). An illustration of the placement of the thermocouples at the side, top and bottom of the pipe is shown in Figure 2.

The logging frequency of the data from the pressure transducers and thermocouples is 100 kHz and 1 kHz, respectively. The high-frequency data are stored from 0.3 s before disk rupture for a 9 s period. After this period, the data from both type of sensors are logged at 50 Hz. The reported initial conditions of the experiments are calculated from the data between 1 ms and 0.5 ms before disk rupture.

2.3. The experiments studied in this work

A series of both full-bore and restricted flow depressurization experiments have been conducted at the ECCSEL depressurization facility (Munkejord *et al.*, 2020a, 2021; Hammer *et al.*, 2022; Log *et al.*, 2024a,b). In the present work, four representative test cases that illustrate the general trends of the temperature evolution in the pipe were chosen to be studied. The tests are summarized in Table 2.

Tests 6 and 8 have been studied previously by Munkejord *et al.* (2020a). Tests 22 and 25 were presented by Log *et al.* (2024a,b), but the temperature data were not studied. Tests 22 and 25 were carried out at colder initial temperatures, and so provide the opportunity to study how the temperature response during decompression varies with the initial temperature of the fluid.

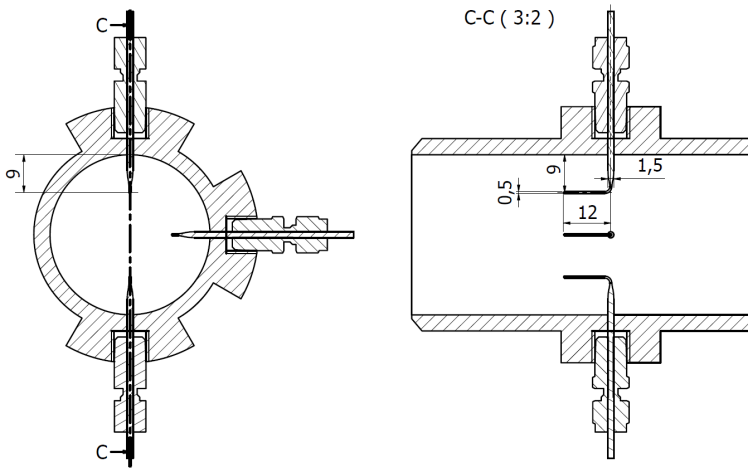

Figure 2: Top-, side- and bottom-mounted temperature sensors. All numbers reported in the figure are in millimetres.

Table 2: Initial conditions of the CO_2 depressurization tests.

Test no.	Pressure avg. (MPa)	Temperature avg. (°C)	Ambient temp. (°C)	Initial mass (kg)
6*	10.40	40.0	6	51
8*	12.22	24.6	9	66
22**	12.48	14.9	14	71
25†	12.27	4.6	−8.5	75

* Munkejord *et al.* (2020a), ** Log *et al.* (2024a), † Log *et al.* (2024b).

3. Models

In this section, the flow models and heat-transfer modelling approach are introduced, and the numerical solution method and boundary conditions are summarized.

3.1. Flow models

3.1.1. The homogeneous equilibrium model

The homogeneous equilibrium model (HEM) consists of the following governing equations for the multiphase mixture flow:

$$\frac{\partial \rho}{\partial t} + \frac{\partial (\rho u)}{\partial x} = 0, \tag{1}$$

$$\frac{\partial (\rho u)}{\partial t} + \frac{\partial (\rho u^2 + p)}{\partial x} = \rho g_x - \mathcal{F}_\mathrm{w}, \tag{2}$$

$$\frac{\partial E}{\partial t} + \frac{\partial ((E+p)u)}{\partial x} = \rho g_x u + \mathcal{Q}. \tag{3}$$

Here, $\rho = \sum_k \alpha_k \rho_k$ is the density of the gas (g), liquid (ℓ) and/or solid (s) mixture, u is the common velocity, p the pressure and E the total energy of the mixture,

$$E = \rho \left(e + \frac{1}{2} u^2 \right), \tag{4}$$

where $e = \sum_k \alpha_k \rho_k e_k$ is the specific internal energy of the mixture and α_k denotes the volume fraction of phase $k \in \{\mathrm{g}, \ell, \mathrm{s}\}$. $\mathcal{F}_\mathrm{w}$ is the pipe wall friction and $\mathcal{Q}$ is the heat transferred through the pipe

wall. g_x is the gravitational acceleration in the axial direction of the pipe. We assume that the pipe is completely horizontal such that $g_x = 0$.

The wall friction is calculated using the Friedel (1979) correlation. The heat-transfer model is described in Section 3.2.

3.1.2. The two-fluid model

The two-fluid model allows the liquid and gas phases to travel at different velocities, $u_g \neq u_\ell$. When solid forms, we assume that it is in homogeneous equilibrium with the gas phase, travelling at the speed of the gas. The governing equations of the model are:

$$\frac{\partial \alpha_{g,s}\rho_{g,s}}{\partial t} + \frac{\partial (\rho_{g,s}u_g)}{\partial x} = \Gamma, \tag{5}$$

$$\frac{\partial (\alpha_\ell \rho_\ell)}{\partial t} + \frac{\partial (\alpha_\ell \rho_\ell u_\ell)}{\partial x} = -\Gamma, \tag{6}$$

$$\frac{\partial (\alpha_{g,s}\rho_{g,s}u_g)}{\partial t} + \frac{\partial (\alpha_{g,s}\rho_{g,s}u_g^2)}{\partial x} + \alpha_{g,s}\frac{\partial p}{\partial x} + \phi_i = u_i\Gamma + \alpha_{g,s}\rho_{g,s}g_x - \mathcal{F}_{wg}, \tag{7}$$

$$\frac{\partial (\alpha_\ell \rho_\ell u_\ell)}{\partial t} + \frac{\partial (\alpha_\ell \rho_\ell u_\ell^2)}{\partial x} + \alpha_\ell \frac{\partial p}{\partial x} - \phi_i = -u_i\Gamma + \alpha_\ell \rho_\ell g_x - \mathcal{F}_{w\ell}, \tag{8}$$

$$\frac{\partial (E_{g,s} + E_\ell)}{\partial t} + \frac{\partial ((E_{g,s} + \alpha_{g,s}p)u_g)}{\partial x} + \frac{\partial ((E_\ell + \alpha_\ell p)u_\ell)}{\partial x} = \alpha_{g,s}\rho_{g,s}g_x u_g + \alpha_\ell \rho_\ell g_x u_\ell + \mathcal{Q}. \tag{9}$$

Here, g, s is used to denote the gas–solid mixture:

$$\alpha_{g,s}\rho_{g,s} = \alpha_g\rho_g + \alpha_s\rho_s, \tag{10}$$

$$\alpha_{g,s} = \alpha_g + \alpha_s, \text{ and } E_{g,s} = E_g + E_s. \tag{11}$$

Note that the above model is identical to the common two-fluid model for liquid and gas until the triple point is reached and solid forms. Once all liquid has dried out in the flow, the model reduces to a pure homogeneous equilibrium model for gas and solid.

In the governing equations, $E_k = \rho_k \alpha_k (e_k + 1/2 u_k^2)$ denotes the total energy of phase $k \in \{g, \ell, s\}$. $u_i = 1/2(u_g + u_\ell)$ is the interfacial momentum velocity. This choice of the interfacial momentum velocity has been showed to not produce entropy (Morin, 2012), and to ensure that the mixture kinetic energy is not affected by phase change (Hammer and Morin, 2014). Γ denotes the mass transfer from liquid to gas and/or solid, and is calculated implicitly by enforcing full thermodynamic equilibrium (pressure, temperature and chemical potential) between the phases. ϕ_i denotes interfacial momentum exchange and is modelled by

$$\phi_i = \Delta p_i \frac{\partial \alpha_g}{\partial x} + \mathcal{F}_i, \tag{12}$$

where Δp_i is the difference between the average bulk pressure and the average interfacial pressure and $\mathcal{F}_i$ is the interface friction. We take

$$\Delta p_i = 1.2 \frac{\alpha_g \rho_g \alpha_\ell \rho_\ell}{\alpha_\ell \rho_g + \alpha_g \rho_\ell} (u_g - u_\ell)^2, \tag{13}$$

following Stuhmiller (1977); Bestion (1990). At the triple point, where all the phases can coexist, we substitute α_g with $\alpha_{g,s}$ and ρ_g with $\rho_{g,s}/\alpha_{g,s}$ in Equations (12)-(13).

The heat-transfer model is described in Section 3.2, and is here modelled in the same way as for the HEM, similarly to the approach of Brown *et al.* (2014). To close the model, we need relations for the gas-to-wall friction $\mathcal{F}_{wg}$, liquid-to-wall friction $\mathcal{F}_{w\ell}$ and the interface friction $\mathcal{F}_i$. These depend on the geometry of the flow. In the present work, two friction models are tested: the Spedding and Hand (1997) friction model for co-current stratified flows, and a flow-regime-map-based friction model.

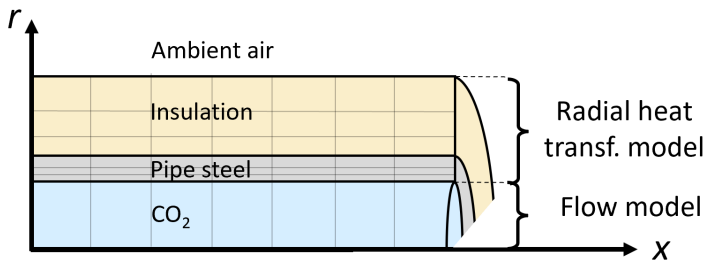

Figure 3: Illustration of the computational domains for the flow model and the heat transfer model.

The flow regimes are based on a simplified version of the RELAP5/MOD3.3 flow regime map (RELAP5 Development Team, 2001; RELAP5, 2001), where we ignore slug flow.

RELAP was developed for water-steam flows in cooling systems for nuclear reactors, but its correlations are formulated such that the properties of different fluids can be applied. The correlations may or may not be accurate for CO_2. The Spedding and Hand model was chosen to illustrate the effect of a large amount of slip between the liquid and gas, while the RELAP model accounts for lower slip during well-mixed flow regimes such as bubbly and mist flows. The friction models are described in more detail in Appendix B.

3.1.3. Treatment of the solid phase

In the HEM, the solid phase is assumed to be in thermal equilibrium with the other phase(s) present, and to be advected at the same velocity.

For the TFM, we assume that once solid forms, it is advected with the speed of the gas phase. This is due to the solid mainly coexisting with the gas phase for the pipe depressurization cases considered here. The gas–solid mixture is assumed to be in equilibrium, and the heat and friction models treat the gas–solid mixture as a single flow field with a mixture volume fraction and density, similarly to the HEM approach.

The models do not account for deposition of the solid phase, or temperature non-equilibrium between the solid and other phases. This may be improved upon in further work.

3.2. Heat-transfer model

The heat transferred through the pipe wall is calculated by solving the heat equation in the radial direction in a two-layer domain, following the method of Aursand *et al.* (2017). The first layer represents the pipe metal, and the second layer represents the insulation. A conceptual overview of the fluid-flow computational domain and the heat-transfer computational domain for a pipe segment is illustrated in Figure 3. Since the length of the pipe is significantly longer than its thickness, the axial heat conduction is negligible compared to the radial heat conduction in the pipe, and it is therefore ignored in this work. We find in our calculations that the axial temperature gradients, even at the ends of the pipe, are typically 100 times smaller than the radial ones. This indicates that it is reasonable to neglect the axial heat conduction.

The heat equation in the radial direction is:

$$\rho(r)c_p(r)\frac{\partial T}{\partial t} - \frac{1}{r}\frac{\partial}{\partial r}\left(r\kappa\frac{\partial T}{\partial r}\right) = 0, \tag{14}$$

where ρ is the density, c_p is the specific heat capacity, and κ is the thermal conductivity of the material. The heat transfer characteristics of the pipe metal and insulation is provided in Table 1.

The heat flux per fluid volume at the inner wall of the pipe is

$$Q = \frac{2}{r_i}h_i(T_{\mathrm{w,i}} - T), \tag{15}$$

Table 3: Saturated boiling heat-transfer correlations tested in this work.

Reference	Label
Gungor and Winterton (1987)	GW
Liu and Winterton (1991)	LW
Steiner and Taborek (1992)	ST
Fang (2013)	Fang

where r_i is the inner radius of the pipe, h_i is the inner wall heat-transfer coefficient and $T_\mathrm{w,i}$ is the temperature at the inner wall of the pipe. At the outer wall, we take the heat-transfer coefficient to be $4\,\mathrm{W\,m^{-2}\,K^{-1}}$. This value has been calculated previously for the experimental setup considered (Munkejord *et al.*, 2020a). As an initial condition, we set the steady-state temperature profile through the pipe steel and insulation, based on the initial temperatures and heat transfer coefficients inside and outside the pipe.

The in-pipe heat-transfer coefficient is estimated based on the Dittus-Boelter correlation (see e.g. Bejan, 1993, Chap. 6), for single phase flows. To account for the enhanced heat transfer due to boiling during the two-phase flow, a set of correlations are tested. These are presented in Table 3. Note that the Steiner and Taborek (1992) correlation was developed and validated for vertical flows. However, it was applied by Collard (2015) for horizontal CO_2 flow during depressurization, and reasonable agreement with wall temperature measurements was found.

Because some of the heat flux correlations are implicitly formulated,

$$\mathcal{Q} = \mathcal{Q}(h_i(\mathcal{Q}), T_\mathrm{w}, T), \tag{16}$$

we calculate the heat-transfer coefficient explicitly based on the fluid solution at time step n and the heat flux from time step $n-1$ (Munkejord and Hammer, 2015). In the simulation code, we enforce an upper limit on the heat-transfer coefficient of $50.000\,\mathrm{W\,m^{-2}\,K^{-1}}$ to avoid numerical difficulties with the explicit solver. For such high heat-transfer coefficients, near perfect thermal contact between the fluid and the wall is obtained, and the sensitivity to the heat-transfer coefficient is low.

In the following, we test these correlations against the simplest alternative, which is to only account for the convective heat transfer using the Dittus-Boelter correlation. When the Dittus-Boelter correlation is applied for two-phase flow, we apply volume averaging for the thermal conductivity k and kinematic viscosity ν, and mass averaging for the specific heat C_p:

$$k = \frac{k_g \alpha_g + k_\ell \alpha_\ell}{\alpha_g + \alpha_\ell}, \tag{17}$$

$$\nu = \frac{\nu_g \alpha_g + \nu_\ell \alpha_\ell}{\alpha_g + \alpha_\ell}, \tag{18}$$

$$C_p = C_{p,g} x_g + C_{p,\ell} x_\ell + C_{p,s} x_s, \tag{19}$$

where $x_k = \frac{\alpha_k \rho_k}{\rho}$ denotes the mass fraction of phase $k \in \mathrm{g}, \ell, s$. The Dittus-Boelter approach for two-phase flow is labelled "conv" in the results section, as it only accounts for convective heat transfer. This approach is also used for gas–solid flow. With the above approach, we assume that the gas–solid viscosity and thermal conductivity are equal to those of the pure gas phase.

3.3. Thermophysical property models

The thermodynamic properties of the two-phase mixture are obtained using the Span and Wagner (1996) equation of state (EOS). To include the description of the solid phase at the sublimation curve, the auxiliary equation of Span and Wagner for the sublimation pressure was combined with the Clapeyron equation to get an equation of state for solid in equilibrium with gaseous CO_2 (Hammer *et al.*, 2013). The fluid thermal conductivity and dynamic viscosity are calculated using the models of Vesovic *et al.* (1990) and Fenghour *et al.* (1998), respectively. The gas–liquid interfacial surface tension is modelled using the correlation of Rathjen and Straub (1977).

3.4. Numerical methods

Both the HEM and the TFM are discretized in space using the robust FORCE (first-order centred) scheme (Toro and Billett, 2000), and in time using the explicit Euler scheme. In order to handle the strong source terms which can be present in the TFM due to friction, Godunov splitting is applied (LeVeque, 2002, Ch. 17). Herein, for each time step, the calculation is split in two. The homogeneous system of equations without the source terms is solved first, and the remaining ODE adding the sources is solved afterwards. If the friction term is large enough to lead to flow reversal during the time step, the time step size is reduced and the ODE calculation adding the friction terms is repeated until the overall time step of the simulation is reached. Splitting is not needed for the HEM, but it is still applied to ensure a fair comparison between the HEM and the TFM results. The models are implemented in our in-house numerical flow-modelling framework.

3.5. Boundary and initial conditions

The initial condition of the fluid in the pipe is assumed to be stagnant ($u = 0$), with constant temperature T and pressure p along the length of the pipe. The full state of the CO_2 in all grid cells is calculated from the experimental pressure and temperature measured before the opening of the rupture disk.

The boundary conditions are set using a ghost-cell approach (see LeVeque, 2002, Chap. 7) At the closed end of the pipe, the boundary condition $u = 0$ is set. This is enabled by a mirror ghost cell. At the open end, a Bernoulli-choking-pressure boundary condition (BBC) is applied. This boundary condition (BC) has been found to perform well at reduced computational cost as compared to, e.g., characteristics-based boundary conditions (Munkejord and Hammer, 2015).

The BBC involves the calculation of the choking pressure at the outflow boundary given that it will be homogeneous, isentropic, quasi-steady, and in thermodynamic equilibrium. The pressure is then set in the ghost cell, and the entropy and flow speed(s) are extrapolated from the inner domain. If the flow does not choke before atmospheric pressure is reached, the atmospheric pressure is set in the ghost cell instead. The full thermodynamic state in the ghost cell is calculated using a pressure-entropy equilibrium flash calculation. More details on the method of calculating the Bernoulli choking pressure can be found in Munkejord and Hammer (2015).

The BBC is a priori written for homogeneous flow. However, when employing this BC for the TFM, we allow for slip by extrapolating the velocities of each phase from the inner domain into the ghost cell. The BC is therefore considered reasonable for both flow models.

Because the BC sets the choking *pressure* in the ghost cell, but extrapolates the flow *speed* from inside the pipe, supersonic flow can be reached at the pipe outlet. This is the case when the outflow state passes through the triple point, where the mixture speed of sound is zero. With the choking-pressure BC, no special treatment is needed to handle outflow at the triple point.[2]

4. Results and discussion

In this section, we compare the different experiments with focus on the temperature evolution in the pipe, highlighting general trends. We then compare model predictions to the experimental measurements. First, the different heat-transfer correlations for boiling flows are compared for the HEM. Next, the HEM and TFM are compared, assessing the effect of slip on the temperature prediction in the pipe.

[2] Similarly, inside the computational domain, there is no special treatment at the triple point – the flow will simply become supersonic.

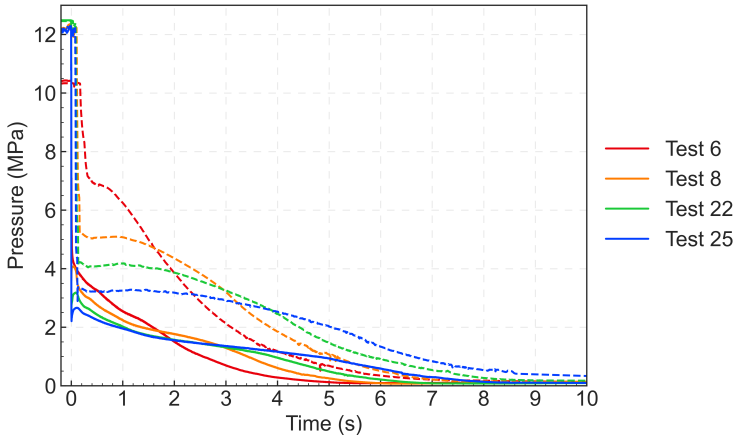

Figure 4: Pressure evolution in the pipe for Tests 6, 8, 22 and 25 at 28 cm (solid lines) and 50 m (dashed lines) from the open end of the pipe.

4.1. Experimental results

Figure 4 shows the pressure evolution during 10 s in the pipe for the decompression tests, measured at 28 cm and 50 m from the open end of the pipe. The pressure response during the first milliseconds of the flow and non-equilibrium effects have been studied in detail by Log *et al.* (2024a); Log (2023). This is relevant for the prediction of running ductile fracture in pipes, where the pressure at the crack tip must be estimated accurately.

The fluid is initially in a dense or liquid phase. Immediately after the disk rupture, the pressure abruptly decreases at the open end of the pipe (solid lines). The flow then transitions to two-phase flow, where the negative spike in pressure seen following the abrupt pressure drop for Test 25 is related to delayed bubble nucleation. After a short time, the depressurization wave has propagated towards the closed end of the pipe (dashed lines). The pressure remains relatively high during some seconds at $x = 50$ m, sustained by the boiling liquid while the pipe is emptied. After around 10 s, atmospheric pressure has been reached along the length of the pipe. The depressurization lasts the longest for the coldest test, Test 25, and the shortest for the warmest test, Test 6. This is reasonable, as the density of the CO_2 is higher for colder initial conditions, so more CO_2 is released for the colder tests. Based on the initial conditions of the tests, the pipe contained approximately 51 kg CO_2 for Test 6 and 75 kg for Test 25. In addition, the two-phase flow has a lower speed of sound closer to the triple point than the critical point of a fluid. The flow in Test 25 therefore likely chokes at a lower flow speed than in Test 6.

The temperature evolution at different positions in the pipe are shown in Figures 5a–5e. These were measured at the side of the pipe, as illustrated in Figure 2. Figure 5a is for the position 8 cm from the open end. As shown, for all the test cases, there are four clear trends in the temperature evolution:

1. Expansion cooling: Due to the abrupt single-phase decompression, there is a sharp temperature drop.

2. Two-phase flow: The temperature drop slows down during the two-phase flow decompression, but accelerates before dry-out. This is most pronounced for the cold experiments. The acceleration in the temperature drop towards dry-out is a consequence of the thermodynamic state of the flow following the saturation curve. For lower pressures along the saturation line, there is a larger temperature decrease for a given pressure reduction.

3. Dry-Out: The liquid dries out and only gas remains. There is no longer latent heat used for phase change so the heat transfer from the pipe wall increases the temperature of the gas.

4. As atmospheric pressure is approached at the open end of the pipe, the flow slows down causing less heat transfer through forced convection. The temperature rise then slows down.

Similar features are also seen in the temperature evolution further inside the pipe. At 15 m from the open end, a second cooling occurs after the dry-out for Test 25, as shown in Figure 5b. A similar second cooling has been observed in previous work (see Munkejord *et al.*, 2021, Fig. 12), and was found to be caused by dry-ice formation upstream which subsequently sublimated and cooled the gas. Further inside the pipe, a second cooling is also seen for Test 22 (Figure 5c) and Test 8 (Figure 5d).

Figure 5e shows the temperature measured at the closed end of the pipe, by the sensor mounted at the side of the pipe. At this position, the cooling during expansion of the two-phase mixture brings the CO_2 to the triple-point temperature where dry ice forms. The dry ice formation is seen as a kink in the temperature measurements.

In Figure 6, the temperature measurements at the bottom of the pipe at the closed end are plotted over 600 s. Here, Test 8, 22 and 25 reach a temperature of −78 °C, which is the sublimation temperature of CO_2 at atmospheric pressure. For Test 8 and Test 22, the temperature increases after around 30–40 seconds. However, the temperature remains at −78 °C over several hundred seconds for Test 25. The long-lasting low temperature is interrupted by a temperature increase at around 100 s to 270 s, likely caused by difficult-to-predict shifts in the position of the sublimating dry ice.

Based on the experimental temperature measurements, we note three main interesting results:

1. The cooling and dry-out occur more slowly for the colder tests due to the additional amount of CO_2 present in the pipe (higher initial density).

2. Despite the tests having initial temperatures from 4.6 °C to 40.0 °C, the minimum temperature reached at different positions in the pipe was similar for all tests.

3. At the open end, the lowest temperature reached was roughly –60 °C for all the experiments, while the coldest temperature reached at the closed end of the pipe was −78 °C, the CO_2 sublimation temperature at atmospheric pressure.

4. The main difference in the temperature evolution for the different tests was related to the formation of dry ice, with the coldest initial condition test remaining at −78 °C at the closed end of the pipe for several hundred seconds.

For the warmest test, thermodynamic flash calculations show that an isentropic decompression to atmospheric pressure would lead to a mass fraction of solid of 0.36, while for the coldest test it would lead to a mass fraction of 0.48.

At the closed end of the pipe, there is little flow. The temperature reached here is therefore mainly determined by the phase-change thermodynamics and slow heat transfer between the fluid and the wall. Similar low temperatures would also be observed at a closed shutoff valve during a depressurization. The minimum temperatures reached is therefore informative when considering which materials should be chosen for the design of CO_2-carrying pipelines and their safety features.

4.2. Model analysis and comparison to experiments

In this section, the simulation results obtained by the flow models with different boiling heat-transfer correlations and slip relations are analysed and compared to the experimental data. For all the simulations presented below, the full length of the pipe is considered, the computational domain is divided into 1200 grid cells, and the Courant-Friedrichs-Lewy (CFL) number determining the time-step length was set to $C = 0.9$.

4.2.1. Comparison of enhanced heat-transfer correlations

In this section, the performance of the enhanced heat-transfer correlations for boiling flows are assessed for CO_2 pipe depressurization simulations, comparing the simulation results to experimental data. We choose here to study the depressurization tests with the warmest (Test 6) and coldest (Test 25) initial conditions. For Test 6, we also show the result if no heat-transfer is applied in the model. The homogeneous equilibrium model (HEM) is employed for the simulations.

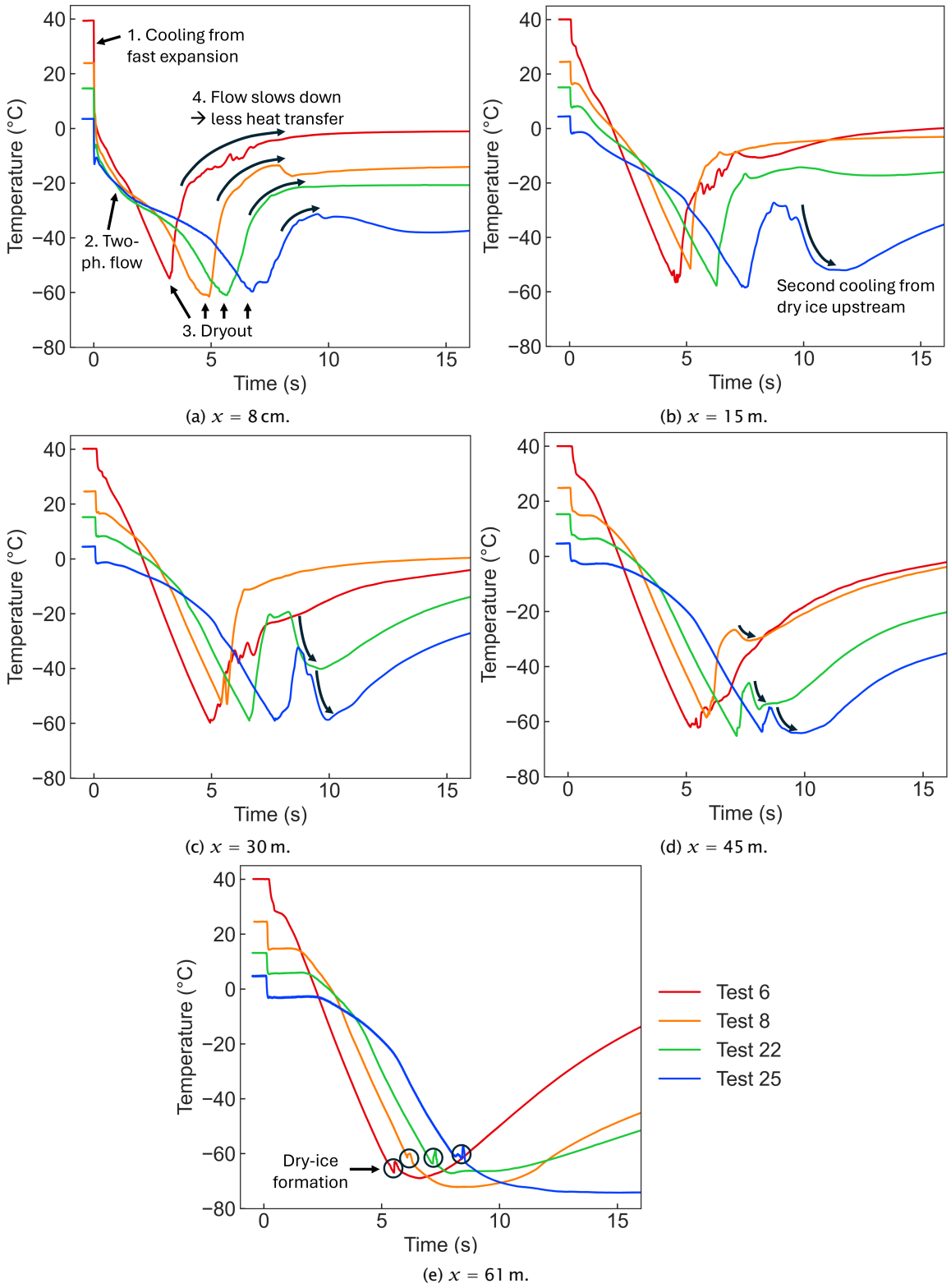

(a) $x = 8$ cm. (b) $x = 15$ m.

(c) $x = 30$ m. (d) $x = 45$ m.

(e) $x = 61$ m.

Figure 5: Temperature measurements for Tests 6, 8, 22 and 25 at the side of the pipe and different positions with respect to the open end.

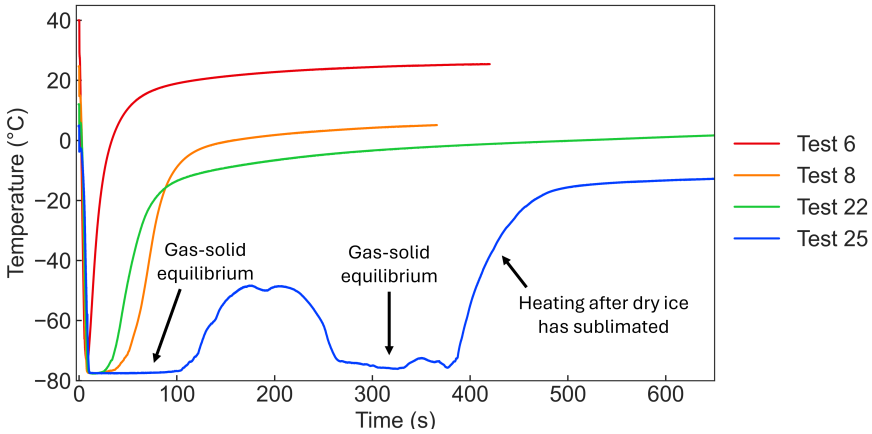

Figure 6: Temperature measurements for Tests 6, 8, 22 and 25 at the bottom of the pipe, $x = 61$ m from the open end.

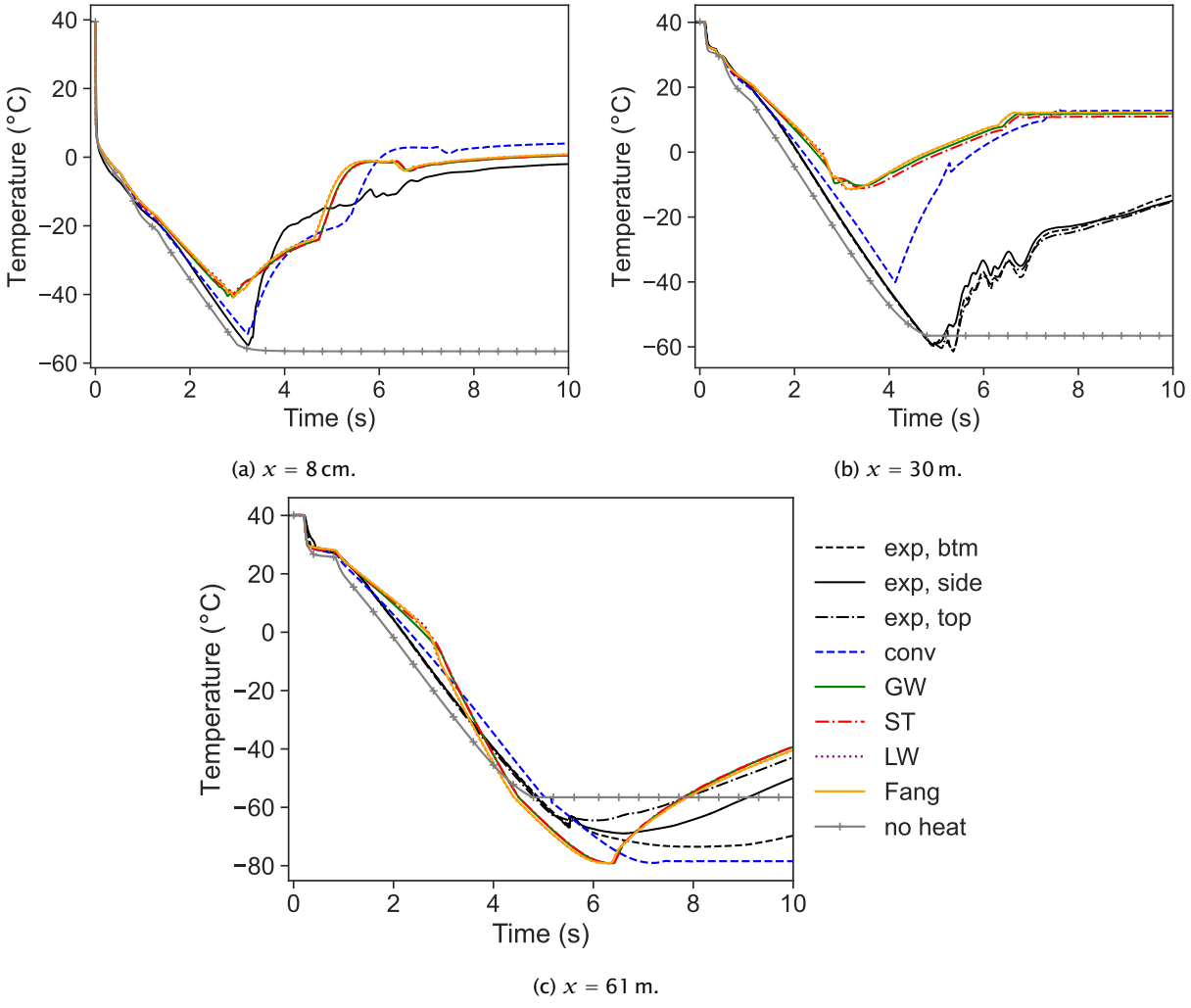

(a) $x = 8$ cm.

(b) $x = 30$ m.

(c) $x = 61$ m.

Figure 7: Comparison of temperature predicted by the HEM with different heat-transfer correlations, and experimental measurements for Test 6 at different axial positions.

For Test 6, Figure 7 shows the predicted temperature for the various models over time near the open end of the pipe (a), the middle of the pipe (b) and near the closed end of the pipe (c), compared to experimental measurements. The corresponding heat-transfer coefficient calculated at these positions for the various models are reported in Figure 8.

As shown in Figure 7, all the simulations with boiling enhancement for the heat transfer between the fluid and the pipe wall obtain nearly overlapping temperature estimates. These simulations predict a too early dry-out. In particular, in the middle of the pipe, the temperature is overpredicted by approximately 50 °C due to the too early dry-out. When no boiling enhancement is considered for the heat transfer coefficient, the dry-out time and temperature is predicted well close to the open end. This is in agreement with the results of Bhuvankar *et al.* (2023), who obtained better agreement for the dry-out than Munkejord *et al.* (2020a) when modelling this test with a heat transfer correlation for forced convection only. However, ignoring enhanced heat transfer during boiling leads to an overprediction of the temperature after dry-out at the open end (Figure 7a), likely due to a too high wall temperature heating the gas.

Note that even when only convective heat transfer is considered, the dry-out is still predicted too early and at a too high temperature in the middle of the pipe, as shown in Figure 7b. This result is surprising, as ignoring enhanced heat transfer caused by boiling should provide a lower temperature than the measured one.

By comparing Figures 7a and 7b, we see that the measured minimum temperatures are about the same, while the simulated minimum temperatures are significantly higher in the middle of the tube than at the outlet. In our interpretation, this is due to the models predicting a too early dry-out, especially in the middle of the tube.

Near the outlet (Figure 7a), the simulation with no heat transfer obtains a slightly lower temperature than the measured one during the two-phase flow. This is the lowest temperature the HEM can predict during the two-phase flow. After reaching the triple point[3], the temperature prediction remains at the triple-point temperature until the end of the simulation at $t = 10\,\mathrm{s}$. This is due to the large amount of liquid still present in the flow when no heat transfer is included. Ignoring heat transfer therefore clearly provides a too late dry-out compared to experimental measurements.

Provided that the assumptions of the HEM are accurate, the "true" heat transfer during Test 6 must have been somewhere in-between no heat transfer and that obtained by assuming purely convective heat transfer. However, the HEM incorporates several simplifications which may be inaccurate. This includes the assumption of no slip between the phases, and that the phases are in full thermal equilibrium. Furthermore, our 1D description of the flow could lead to inaccurate heat-transfer estimates as the bulk flow properties are used when estimating the near-wall flow properties. Munkejord *et al.* (2020a) suggested that early dry-out could be caused by the no-slip condition of the HEM, leading to a too large outflow of liquid, and that the two-fluid model could match the experimental data better. This is investigated in Section 4.2.2.

In Figure 8, the predicted heat-transfer coefficient is presented for the different heat-transfer correlations. Close to the open end, all the boiling enhancement correlations obtain a heat-transfer coefficient at the upper limit set in the numerical simulation, $50.000\,\mathrm{W\,m^{-2}\,K^{-1}}$. This can be seen in Figure 8a. The prediction of such a high heat transfer coefficient lasts nearly until dry-out is reached in the pipe. The Gungor–Winterton correlation predicts a reduction in the heat-transfer coefficient around 1 s before dry-out is predicted, and Steiner–Taborek around 0.3 s before the dry-out. Nevertheless, the heat-transfer coefficient remains so high that all the models can be considered to predict near perfect thermal contact between the fluid and the pipe wall during the two phase flow in this region of the pipe. It is therefore reasonable that the models obtain nearly overlapping temperature predictions here.

In the middle of the pipe, a similar trend is seen, but the Gungor–Winterton correlation predicts a reduced heat-transfer coefficient at an earlier time than the other correlations. Finally, at the closed end of the pipe, the Steiner–Taborek correlation obtains a significantly lower heat-transfer coefficient than

[3]We remark that in the simulations, no special treatment is needed to capture the behaviour at the triple point.

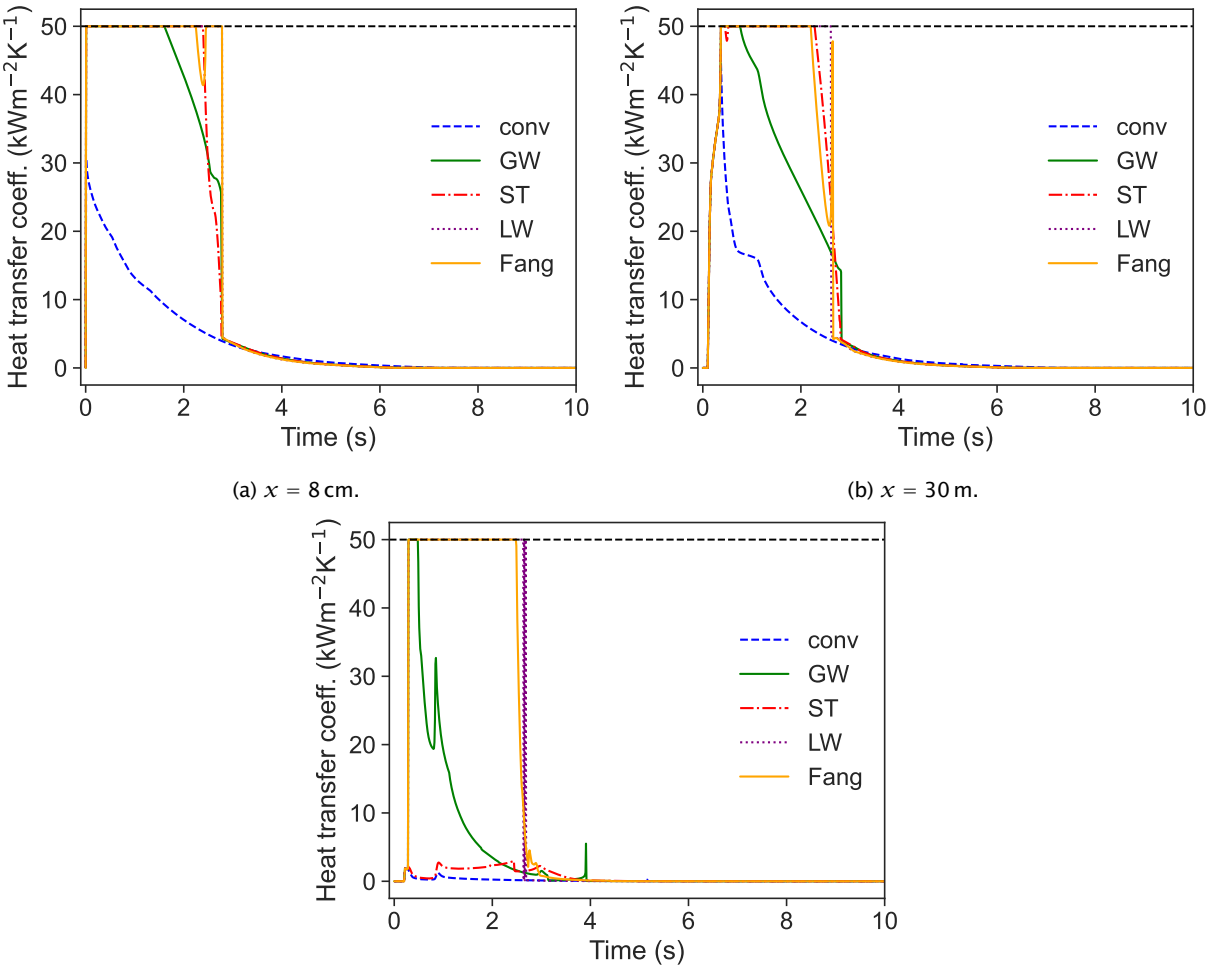

(a) $x = 8\,\mathrm{cm}$.

(b) $x = 30\,\mathrm{m}$.

(c) $x = 61\,\mathrm{m}$.

Figure 8: Comparison of heat-transfer coefficient predicted by the HEM with different correlations, at different axial positions for Test 6.

the others. The Liu–Winterton and Fang correlations both reach the upper limit of $50.000\,\mathrm{W\,m^{-2}\,K^{-1}}$ during two-phase flow and remain there until dry-out is predicted. The oscillations of the Liu–Winterton predictions are related to the disappearance of the liquid phase.

For Test 25, Figure 9 shows the predicted temperature for the various models over time near the open end of the pipe (a), the middle of the pipe (b) and near the closed end of the pipe (c), compared to experimental measurements. The corresponding heat-transfer coefficients at these positions are reported in Appendix A.1. The result found by ignoring heat transfer is not included here, but the same trend was seen for this case as for Test 6 in Figure 7.

For this test, the simulations with the boiling enhancement still perform very similarly during the two-phase flow. As for Test 6, the models predict nearly perfect thermal contact with the wall during the two-phase flow. Close to the open end, the dry-out predicted by the models with boiling enhancement is only slightly delayed compared to the experimental measurement. Employing the purely convective heat-transfer model leads to a too late dry-out, and a much too low temperature before the temperature recovery. The result is similar in the middle of the pipe. The simulations do not reproduce the clear second cooling caused by dry-ice at this position.

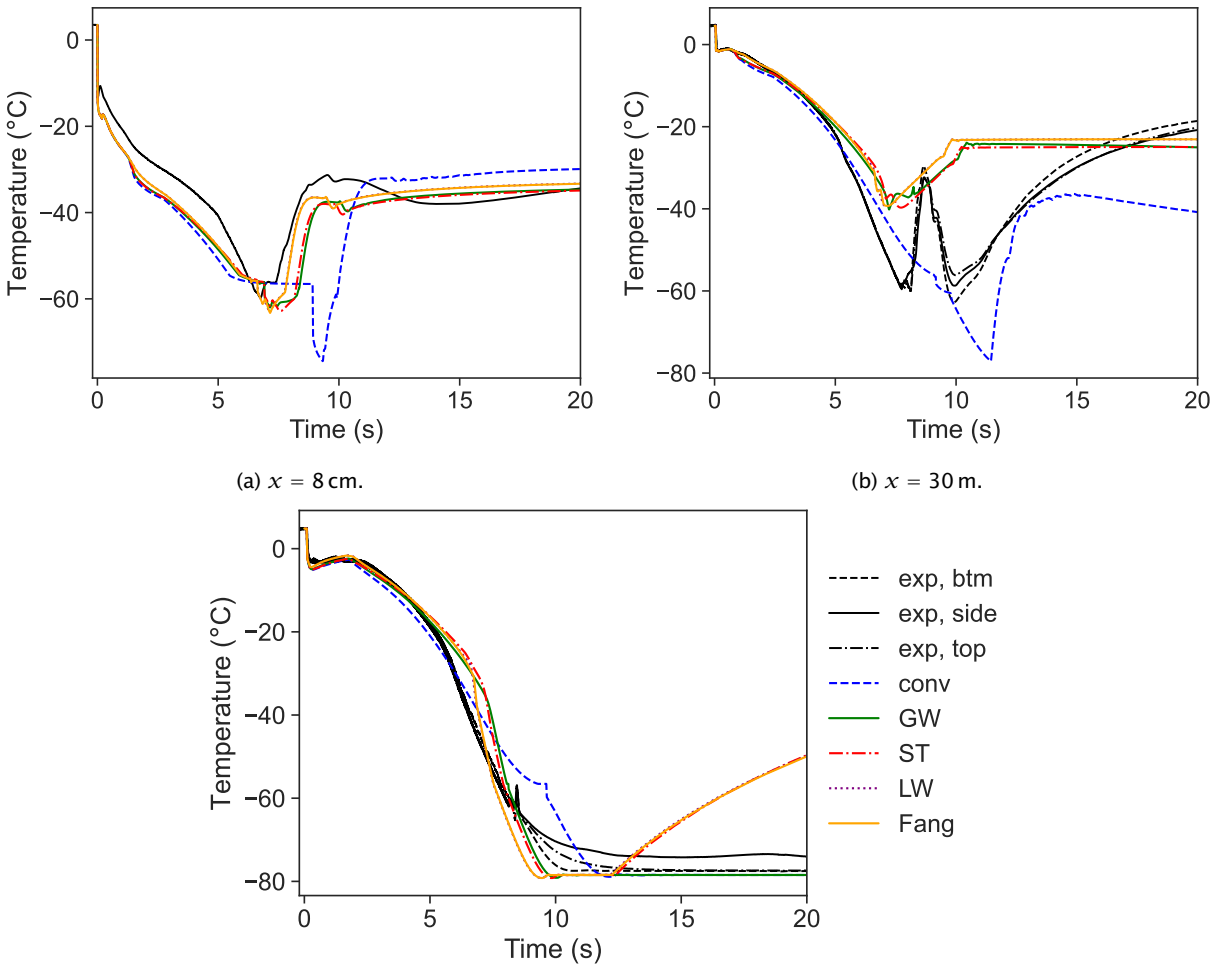

(a) $x = 8$ cm.

(b) $x = 30$ m.

(c) $x = 61$ m.

Figure 9: Comparison of temperature predicted by the HEM with different heat-transfer coefficients, and experimental measurements, at different axial positions, for Test 25.

At the closed end, all the simulations with boiling enhancement provide similar results except the Gungor–Winterton correlation. The Steinar–Taborek, Liu–Winterton and Fang simulations all obtain a too early temperature recovery after reaching the gas–solid equilibrium temperature. The Gungor-Winterton simulation is in better agreement with the experimental measurements. The HEM with no boiling enhancement obtains a clear kink at the triple-point temperature, similar to the kink/oscillations observed in the experimentally measured temperature. For this test, ignoring boiling enhancement does not provide a result which agrees better with the experimental measurements. Thus, the improved result which Bhuvankar *et al.* (2023) found for Test 6 by ignoring boiling enhancement is not general.

Based on the above results, it is clear that:

- All the boiling enhancement heat-transfer correlations perform similarly for CO_2 depressurization when applied with the HEM. None of the models can be said to outperform the others.
- If boiling enhancement is ignored, the calculated temperature is in better agreement with measurements for the warmest test (Test 6), but the result is poorer for the coldest test (Test 25).

We therefore conclude that none of the heat-transfer correlations tested provide fully satisfactory

overall estimates of the temperature evolution in the pipe in conjunction with the HEM. In order to improve temperature estimates, better heat transfer, friction and slip models are likely needed. The assumption of full equilibrium flow may also have to be relaxed. Munkejord *et al.* (2020a) suggested that the temperature predictions, and particularly the dry-out point, may be improved if slip is allowed between the phases. This is explored in the following section by comparing the predictions of the HEM with those of the two-fluid model.

4.2.2. The effect of slip: Two-fluid model vs. the homogeneous equilibrium model

In this section, the simulation results of the HEM and TFM are compared. In Section 4.2.1, all the tested boiling enhancement correlations were found to perform similarly with the HEM. To focus on the effect of including or ignoring slip between the phases, we employ the Gungor and Winterton (1987) correlation for both the HEM and TFM. For the TFM, two different friction models are tested. They are briefly described in Section 3.1.2, and in more detail in Appendix B. The RELAP-based model accounts for multiple two-phase flow regimes including bubbly, annular, mist and stratified flows, while the Spedding and Hand model assumes stratified two-phase flow. The latter assumption will only hold for a small segment of the pipe, but we still include the Spedding and Hand model, as this is a relatively easy way to test the effect of phase slip.

Once again, we focus on Test 6 and Test 25, the experiments with the warmest and coldest initial conditions, respectively. The results are representative for the remaining tests as well.

First, consider Test 6, with the warmest initial condition. Figure 10 shows the predicted temperature of the HEM and TFM over time near the open end of the pipe (a), the middle of the pipe (b) and near the closed end of the pipe (c), compared to experimental measurements. The predicted flow velocity for each phase (TFM) and the total mixture (HEM) at these positions are reported in Figure 11.

Close to the open end, and in the middle of the pipe, dry-out is reached almost at the same time for the HEM and the TFM with the RELAP friction model, see Figure 10a. Their results are nearly overlapping. TFM with the stratified friction model obtains dry-out later, in agreement with the hypothesis of Munkejord *et al.* (2020a). Close to the open end of the pipe, TFM with the stratified friction model predicts dry-out at roughly the same time as it occurs in the experiment. However, the predicted dry-out temperature is about 15 °C too high in the simulation. In the middle of the pipe, the TFM with the stratified friction model still obtains dry-out a few seconds too early, and the temperature prediction is much too high, by roughly 40 °C. Even with the relatively large slip of stratified flow, we cannot reproduce the low dry-out temperature. At the closed end of the pipe, the difference between the models and data is smaller. Here, the velocities are low, so little slip is present. The cooling is slower for the stratified model, and is delayed compared to the experimental data. The model also predicts more dry-ice formation than the others, causing it to stay longer at the gas-solid equilibrium temperature at atmospheric pressure.

The velocity plots in Figure 11 show the effect of the friction models; assuming stratified flow throughout the pipe (Sped-Hand), using flow regime maps (RELAP), or assuming fully homogeneous flow (HEM). The stratified model obtains significant slip between the phases, increasing from $50\,\mathrm{m\,s^{-1}}$ to over $100\,\mathrm{m\,s^{-1}}$ close to the open end. Further inside the pipe, the slip is smaller, as the flow velocities are smaller. The velocity spikes for the TFMs occur at the disappearance of the liquid phase. The RELAP-based friction model generally predicts little slip between the phases. As the stratified model predicts such a large slip between the phases, and a much lower liquid velocity than the other models, the mass outflow over time is predicted to be much lower than for the other models. This can be seen more clearly when comparing their predicted pressure evolution with experimental measurements.

In Figure 12, the pressure evolution predicted by the models at three positions along the pipe are compared to experimental measurements. All the models have a tendency of overpredicting the pressure before $t = 3.5\,\mathrm{s}$. However, the TFM with the Spedding and Hand friction model overpredicts the pressure the most. At early times close to the open end, the pressure is overpredicted by up to 10 bar by the stratified model. At later times, at the closed end, the pressure is overpredicted by up to 15 bar. Enforcing stratified flow throughout the pipe restricts the outflow of liquid, which leads

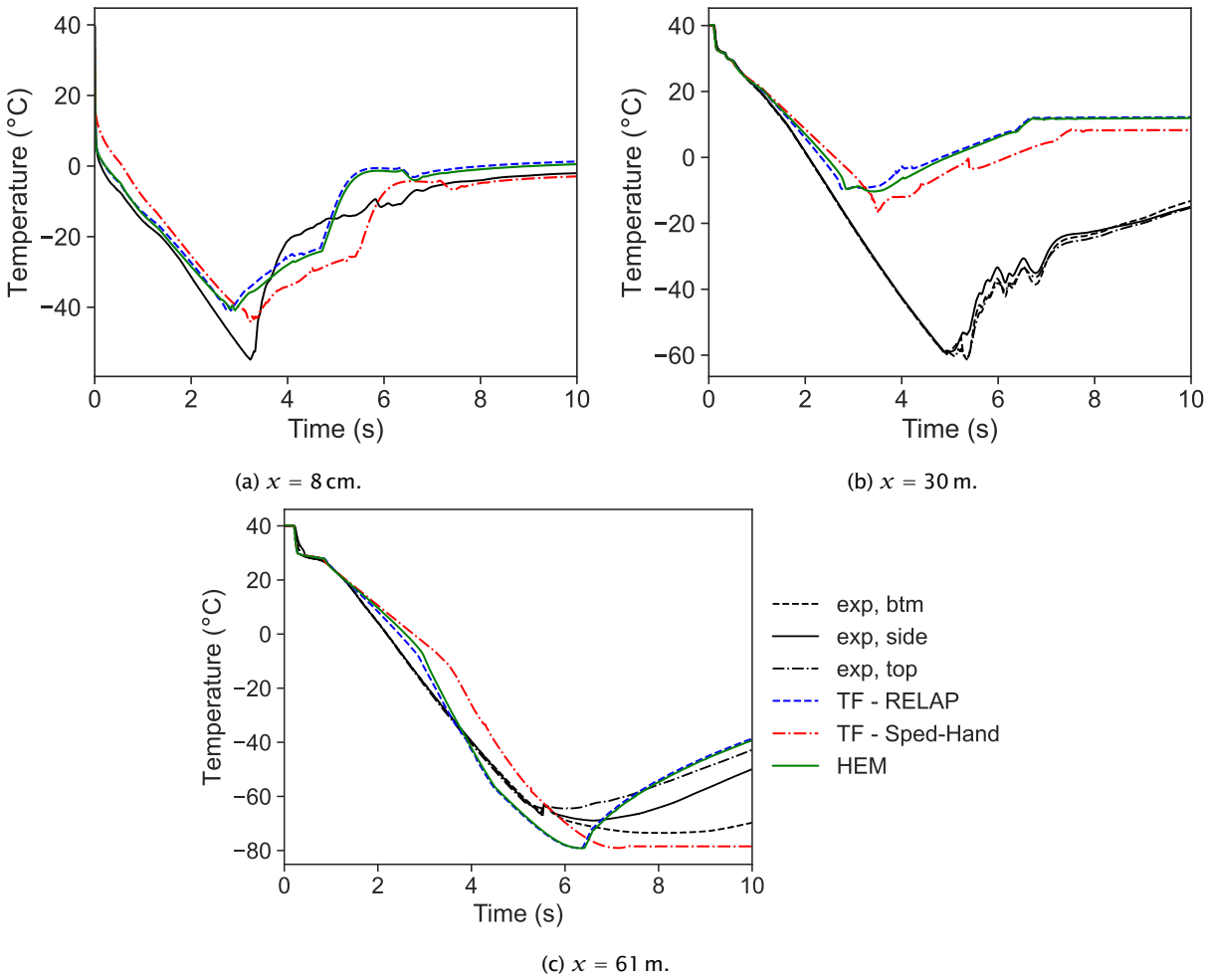

(a) $x = 8$ cm. (b) $x = 30$ m.

(c) $x = 61$ m.

Figure 10: Comparison of temperature predicted by the HEM and TFM, and experimental measurements, at different positions, for Test 6.

to a slower pressure reduction than observed in the experiments. Imposing high slip throughout the two-phase flow improved the predicted dry-out time, but not the pressure predictions.

Let us now consider Test 25, with the coldest initial condition. Figure 13 shows the predicted temperature of the HEM and TFM over time near the open end of the pipe (a), the middle of the pipe (b) and near the closed end of the pipe (c), compared to experimental measurements. The predicted flow velocity for each phase (TFM) and the total mixture (HEM) at these positions are reported in Appendix A.2.

In Figure 13a, close to the open end of the pipe, we see that both the TFM with the RELAP friction and HEM have a tendency of underpredicting the temperature. Both models estimate dry-out at a similar time and temperature as that recorded in the experiment, with the HEM being somewhat delayed. The TFM with Spedding and Hand friction shows a very different trend. Before dry-out, the temperature is overestimated. After dry-out, a chaotic temperature evolution follows with both a second and third cooling. This is related to the prediction of dry ice in the pipe by this model, as shown in Figure 14a.

In the middle of the pipe, both the TFMs capture the second cooling, but it is overpredicted and the following temperature recovery is delayed and cannot be seen in the plot. The TFM assuming stratified flow obtains a slower initial cooling than the RELAP flow-regime-based one. The HEM does not obtain a

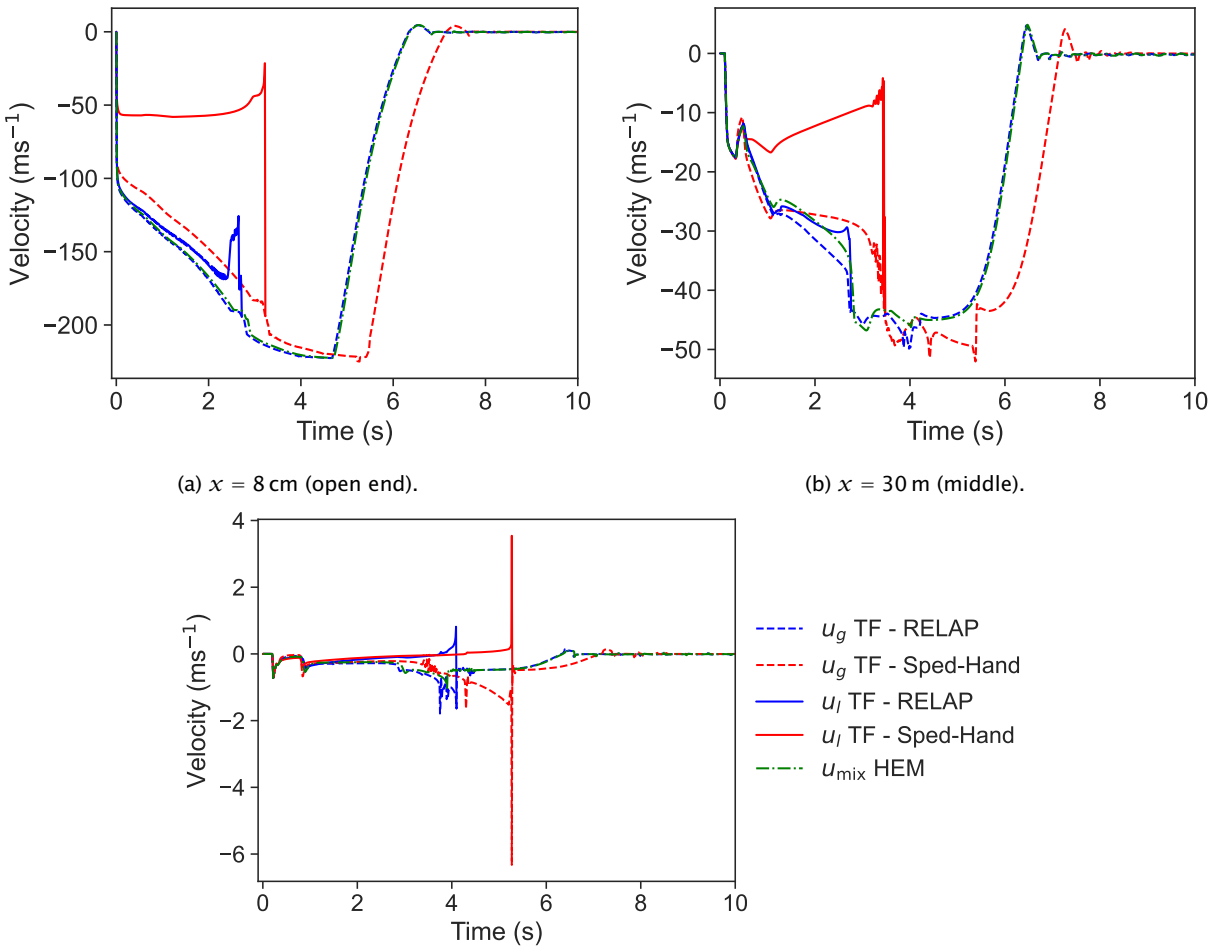

(a) $x = 8$ cm (open end).

(b) $x = 30$ m (middle).

(c) $x = 61$ m (closed end).

Figure 11: Comparison of flow velocity predicted by the HEM and TFM, at different positions, for Test 6.

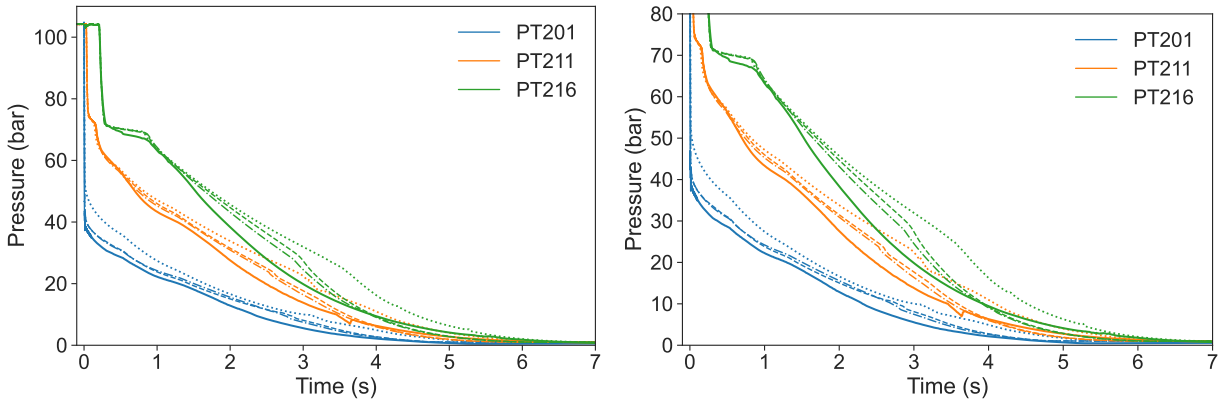

(a) Full pressure evolution

(b) Zoomed in on multiphase flow area

Figure 12: Comparison of pressure predicted by the HEM (dashed), TFM with RELAP friction (dash-dotted), TFM with Spedding and Hand friction (dotted) and experimental measurements (solid) 8 cm (PT201), 9.6 m (PT211) and 61.5 m (PT216) from the open end of the pipe for Test 6.

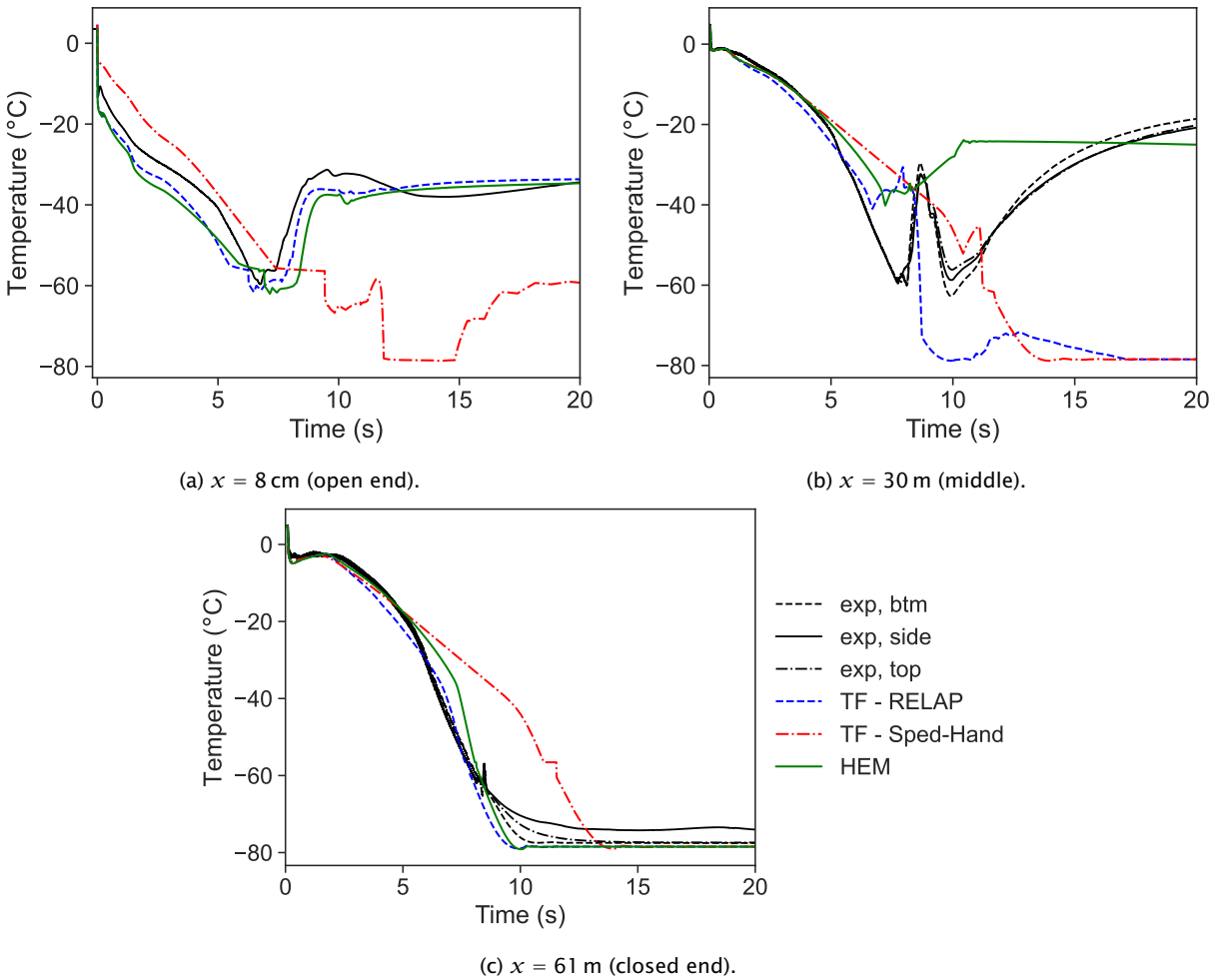

(a) $x = 8$ cm (open end).

(b) $x = 30$ m (middle).

(c) $x = 61$ m (closed end).

Figure 13: Comparison of temperature predicted by the HEM and TFM, and experimental measurements, at different positions, for Test 25.

second cooling. Once again, the temperature evolution is strongly affected by the prediction of dry ice, where the TFMs both predict dry-ice formation causing the second cooling, as shown in Figure 14b.

Finally, at the closed end of the pipe, both the HEM and the TFM with RELAP-friction obtain similar predicted temperatures, which agree with the measured temperature at the bottom of the pipe. A significant amount of dry-ice formation is predicted by the TFM at this position, with a mass fraction up to 40% as shown in Figure 14c. The HEM predicts a much smaller amount, as the low slip in the model leaves less liquid to form the solid phase at the triple point. The TFM with the Spedding and Hand friction model again obtains a delayed cooling, reaching the gas-solid equilibrium temperature about 4 s later than the experimental recordings. This delay is caused by the significant slip obtained in the model close to the open end of the pipe, where the liquid phase is escaping the pipe much slower than the gas phase. This is also why the model predicts more dry ice formation than the others: there is more liquid present at the triple point, which then turns into solid during further depressurization. This model predicts a mass fraction of solid up to nearly 50%, as shown in Figure 14c. The predicted pressure evolution for Test 25 is shown in Appendix A.3.

The TFM with the Spedding and Hand friction model predicts solid formation along the entire pipe due to the slow outflow of the liquid phase. This can be seen in Figure 15, compared to the TFM with

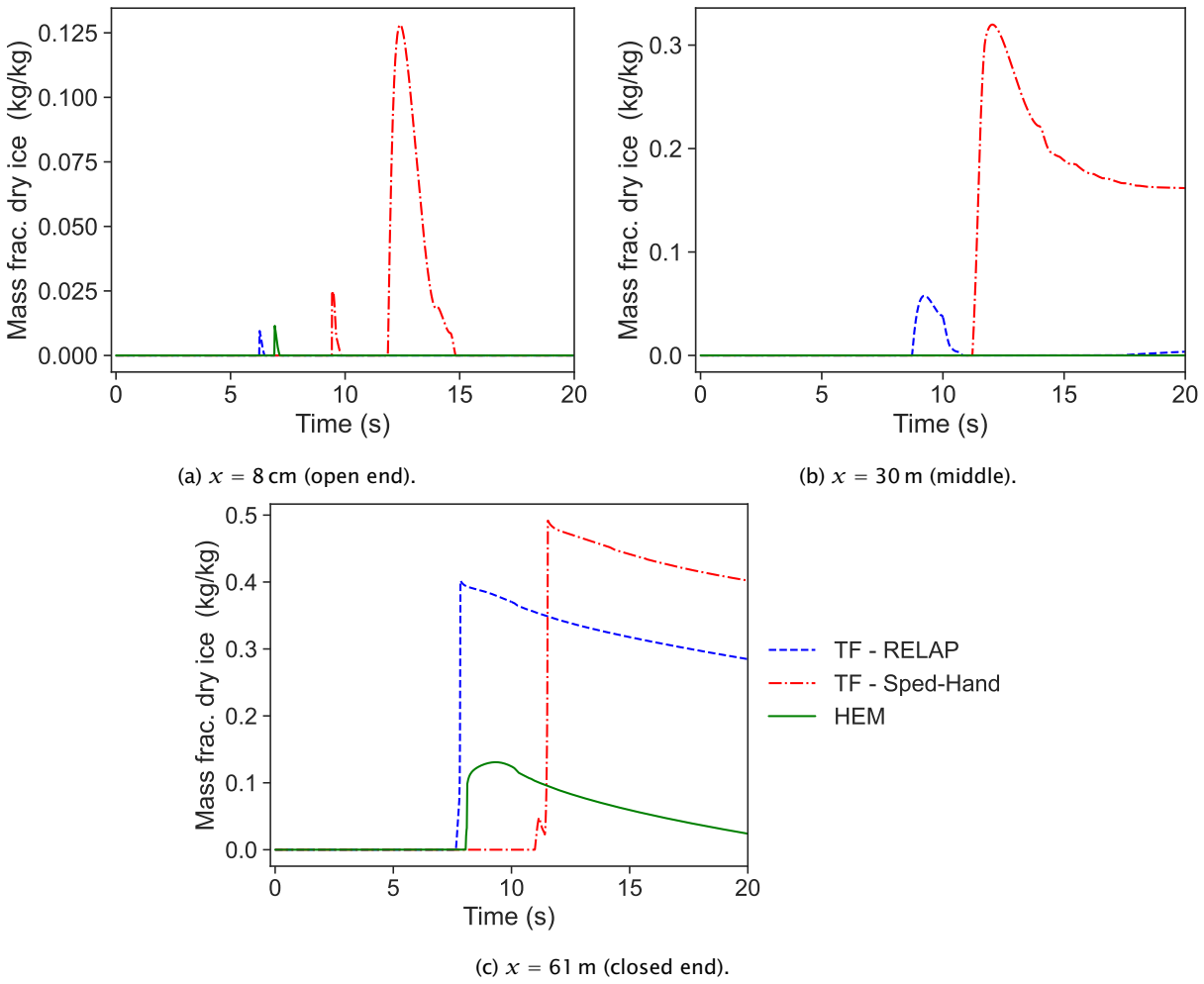

(a) $x = 8$ cm (open end).

(b) $x = 30$ m (middle).

(c) $x = 61$ m (closed end).

Figure 14: Comparison of solid mass fraction predicted by the HEM and TFM, at different positions, for Test 25.

the RELAP friction model. Here, the "isentropic limit" denotes the mass fraction of solid would be produced during an isentropic expansion of the CO_2 from the initial state in the pipe to atmospheric pressure. The presence of dry-ice predicted in the models leads to significant differences in their temperature predictions.

Based on the comparison of the HEM and TFM with different friction models for Test 6 and Test 25 above, we note the following:

- Including significant slip by assuming stratified two-phase flow caused later dry-out, and at a lower temperature – as expected.
- However, the overall temperature and pressure evolution was not predicted well when fully stratified two-phase flow was assumed, because the outflow from the pipe was too low compared to experimental measurements. For Test 25 this led to the prediction of significant dry-ice at the open end, providing a particularly strong underprediction of the temperature.
- The RELAP-type friction model which accounts for more flow regimes (e.g., bubbly, annular, mist) obtained results more similar to those of the HEM. The temperature predictions were not significantly improved, but the model obtained a secondary cooling caused by dry-ice in the

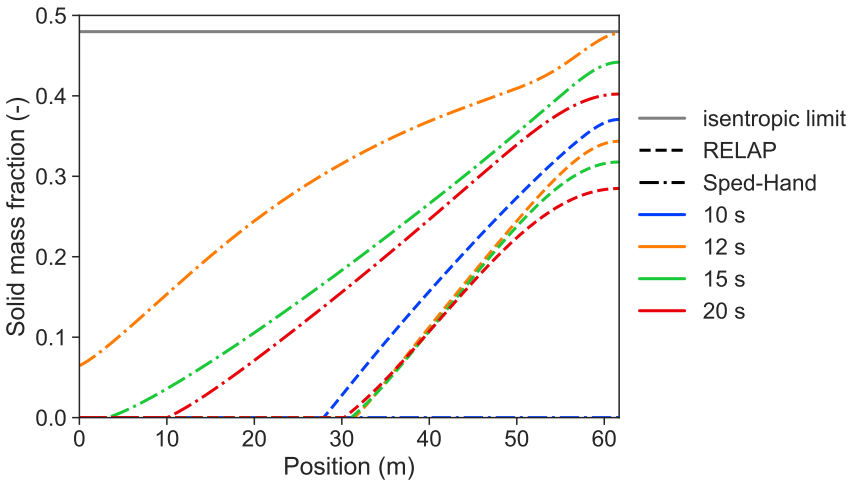

Figure 15: Comparison of solid mass fraction predicted by the TFM, at different times, for Test 25.

middle of the pipe for Test 25, which the HEM did not. The secondary cooling was overestimated compared to experimental data.

4.3. Discussion

Below, we discuss the results focusing on outflow modelling, dry-ice formation and, slip and heat-transfer correlations.

Slightly counter-intuitively, both the HEM and the TFM with RELAP-type friction model performed best near the outlet and near the closed end of the pipe. At the outlet, this is particularly the case during the two-phase flow period, where the flow velocity is high and we expect fully dispersed flow. Although the predicted dry-out temperature was too high, the temperature trend after dry-out matched the experiments reasonably well. At the closed end of the pipe, on the other hand, the flow velocity is low and the temperature is mainly determined by phase change and heat transfer. This was also satisfactorily captured by the models, although the duration of the period affected by dry-ice sublimation is sensitive to the amount and configuration of dry-ice formed.

The predicted pressure and temperature in the flow model strongly depend on how the outflow from the pipe is estimated. In the present work, the HEM choking pressure is set both for the HEM and the TFM. However, for such a rapid depressurization, the phase change often occurs delayed, leading to a lower choking pressure and a higher outflow (Log *et al.*, 2024a,b). Including non-equilibrium phase change could possibly improve the estimated results of the TFM with the Spedding and Hand friction model, which currently predicts too low outflow from the pipe.

The model results further showed that the presence of dry ice significantly affects the temperature predictions in the flow. In all the flow models applied in this work, we assume that once gas–solid flow is present, the solid will be in equilibrium with the gas phase and flow at the speed of the gas. These assumptions would be accurate if the solid is present as small particles dispersed in the gas. However, there could be a temperature non-equilibrium between the gas and solid phases, and the dry-ice may agglomerate and sediment in certain locations in the pipe. This is especially the case for low flow velocities, near the closed end of the pipe.

Though slip plays a part in modelling the flow of CO_2 during depressurization and in predicting dry-out, it does not fully explain the deviation between predicted and observed temperature in the pipe. Even when fully stratified two-phase flow was assumed, the temperature was still significantly overestimated before dry-out for Test 6 (Figure 10). On the other hand, for Test 25, significant slip led to delayed dry-out at a too low temperature (Figure 13). Furthermore, both the RELAP-type slip model and pressure measurements from the pipe point towards lower slip between the phases, especially

close to the open end. Most likely, improving temperature estimates for CO_2 depressurization will require both improved heat-transfer correlations *and* slip models.

In the present model, simplified heat-transfer correlations were applied, assuming either purely convective heat transfer or enhanced boiling heat transfer. It may be necessary to apply flow regime dependent heat-transfer correlations to accurately capture the temperature evolution recorded in the experiments. As noted by several authors, modelling heat transfer for boiling CO_2 flow in pipes is difficult. When testing general heat-transfer correlations for boiling flows, Shah (2006) found that 29 out of the 30 fluids tested showed good agreement with both the Shah (1982) and the Gungor and Winterton (1987) correlations. The only exception was CO_2. Therefore, for CO_2, heat-transfer correlations taking both flow regimes and the particular thermophysical properties into account may be necessary (Cheng *et al.*, 2008a,b, 2021).

Cheng *et al.* (2021) observed that the evaporation heat transfer varied significantly with the saturation temperature. They stated that nucleate boiling was more pronounced at higher saturation temperatures and low vapour fractions. Similar effects were also observed by Lei *et al.* (2020), but they also noted a suppression of heat transfer for high vapour fractions. Interestingly, convective heat transfer has also been found to change significantly in the near-critical region of a fluid, even when the flow is single-phase, as detailed by Hendricks *et al.* (1970). The different heat transfer observed for different saturation temperatures and vapour fractions could contribute to the differences observed between the warmest (Test 6) and coldest (Test 25) experiments. To the authors' knowledge, there are currently no heat-transfer correlations that capture all these variations.

We note that both the HEM and TFM tested assume a temperature equilibrium between the phases. It would be interesting to investigate the effect of temperature non-equilibrium.

5. Conclusion

In the present work, we have analysed the temperature evolution during four full-bore pipe depressurization tests with CO_2 at different initial temperatures, and investigated different fluid dynamics modelling approaches with and without the inclusion of phase slip, and with different heat-transfer models. The experimental data had the same overall trends for different initial temperatures, and the same minimum temperatures were reached at different positions in the pipe. The main difference was related to the timing of these changes, where the experiment with the warmest initial condition had a faster cooling, a faster temperature recovery after dry-out, and less production of dry ice. For the test with the coldest initial condition, the temperature data indicated that dry ice remained at the closed end of the pipe for several hundred seconds.

The experimental data were applied to test different heat-transfer correlations for boiling flows, and the effect of ignoring or including slip between the phases. A set of enhanced heat-transfer correlations were tested with the homogeneous equilibrium model (HEM) for two-phase flow. All the boiling heat-transfer correlations provided similar temperature predictions. These correlations all predicted near-perfect thermal contact throughout the two-phase flow. None of the heat-transfer correlations tested could be said to outperform the others. For the warmest test, ignoring enhanced heat-transfer due to boiling provided the best result compared to experimental data, while for the coldest test the result was the opposite. This indicates that there is a need to take the effect of different saturation temperatures and vapour fractions into account in order to develop more generally applicable heat-transfer correlations.

The effect of slip was also tested using the two-fluid model (TFM), with two different friction models: a RELAP-type model accounting for several flow regimes, and the Spedding and Hand model which assumes stratified flow and high slip. Here, the same model for boiling heat transfer (Gungor–Winterton) was employed for both the TFM and HEM. The TFM with the Spedding and Hand model did obtain a later dry-out than the HEM, but the mass outflow was reduced due to the assumption of high slip at the open end of the pipe. The overall results for the high-slip model was therefore poorer than those of the HEM. The TFM with the RELAP-type friction model performed similarly to the HEM. These models

performed reasonably well at the outlet and at the closed end of the pipe, but they were not able to capture the temperature evolution in the middle of the pipe. This means that from a practical point of view, one might as well use the HEM until more accurate sub-models have been developed for the TFM.

The experimental conditions tested in the current work range from high-speed fully dispersed flow at the outlet to calm, stratified flow conditions at the closed end of the pipe, with strong spatial and temporal pressure and temperature gradients. In addition, the thermodynamic state passed through the critical region during the experiments. The results indicate that common models for phase slip, friction and heat transfer have limited accuracy for such strongly varying flows of CO_2. In particular, the application of specialized flow-regime-dependent heat-transfer models may be needed. Finally, models with temperature non-equilibrium could be tested both for the liquid–gas and gas–solid flows.

Acknowledgments

This publication has been produced with support from the NCCS Centre, performed under the Norwegian research programme Centres for Environment-friendly Energy Research (FME). The authors acknowledge the following partners for their contributions: Aker BP, Allton, Ansaldo Energia, Baker Hughes, CoorsTek Membrane Sciences, Elkem, Eramet, Equinor, Gassco, Hafslund Oslo Celsio, Krohne, Larvik Shipping, Norcem Heidelberg Cement, Offshore Norge, Quad Geometrics, SLB Capturi, Stratum Reservoir, TotalEnergies, Vår Energi, Harbour Energy and the Research Council of Norway (257579).

The construction of the ECCSEL Depressurization Facility was supported by the INFRASTRUKTUR programme of the Research Council of Norway (225868).

Data availability

The experimental data discussed in this study is available at Zenodo (Munkejord *et al.*, 2020b; Log *et al.*, 2023a,b).

References

Aursand, E., Dumoulin, S., Hammer, M., Lange, H. I., Morin, A., Munkejord, S. T., Nordhagen, H. O., Sep. 2016. Fracture propagation control in CO_2 pipelines: Validation of a coupled fluid-structure model. *Eng. Struct.* 123, 192–212. doi:10.1016/j.engstruct.2016.05.012.

Aursand, P., Hammer, M., Lavrov, A., Lund, H., Munkejord, S. T., Torsæter, M., Jul. 2017. Well integrity for CO_2 injection from ships: Simulation of the effect of flow and material parameters on thermal stresses. *Int. J. Greenh. Gas Con.* 62, 130–141. doi:10.1016/j.ijggc.2017.04.007.

Aursand, P., Hammer, M., Munkejord, S. T., Wilhelmsen, Ø., Jul. 2013. Pipeline transport of CO_2 mixtures: Models for transient simulation. *Int. J. Greenh. Gas Con.* 15, 174–185. doi:10.1016/j.ijggc.2013.02.012.

Bejan, A., 1993. *Heat Transfer*. John Wiley & Sons, Inc., New York. ISBN 0-471-50290-1.

Bestion, D., Dec. 1990. The physical closure laws in the CATHARE code. *Nucl. Eng. Design* 124 (3), 229–245. doi:10.1016/0029-5493(90)90294-8.

Bhuvankar, P., Cihan, A., Birkholzer, J., Jul. 2023. A framework to simulate the blowout of CO_2 through wells in geologic carbon storage. *Int. J. Greenh. Gas Con.* 127, 103921. doi:10.1016/j.ijggc.2023.103921.

Biberg, D., 1999. An explicit approximation for the wetted angle in two-phase stratified pipe flow. *Can J Chem Eng* 77, 1221–1224. doi:10.1002/cjce.5450770619.

Brown, S., Beck, J., Mahgerefteh, H., Fraga, E. S., 2013. Global sensitivity analysis of the impact of impurities on CO_2 pipeline failure. *Reliab. Eng. Syst. Safe* 115, 43–54. doi:10.1016/j.ress.2013.02.006.

Brown, S., Martynov, S., Mahgerefteh, H., Chen, S., Zhang, Y., 2014. Modelling the non-equilibrium two-phase flow during depressurisation of CO_2 pipelines. *Int. J. Greenh. Gas Con.* 30, 9–18. doi:10.1016/j.ijggc.2014.08.013.

Cao, Q., Yan, X., Guo, X., Zhu, H., Liu, S., Yu, J., Jul. 2018. Temperature evolution and heat transfer during the release of CO_2 from a large-scale pipeline. *Int. J. Greenh. Gas Con.* 74, 40–48. doi:10.1016/j.ijggc.2018.04.015.

Cao, Q., Yan, X., Liu, S., Yu, J., Chen, S., Zhang, Y., 2020. Temperature and phase evolution and density distribution in cross section and sound evolution during the release of dense CO_2 from a large-scale pipeline. *Int. J. Greenh. Gas Con.* 96, 103011. doi:10.1016/j.ijggc.2020.103011.

Cheng, L., Ribatski, G., Quibén, J. M., Thome, J. R., 2008a. New prediction methods for CO_2 evaporation inside tubes: Part I – A two-phase flow pattern map and a flow pattern based phenomenological model for two-phase flow frictional pressure drops. *Int. J. Heat Mass Tran.* 51 (1–2), 111–124. doi:10.1016/j.ijheatmasstransfer.2007.04.002.

Cheng, L., Ribatski, G., Quibén, J. M., Thome, J. R., 2008b. New prediction methods for CO_2 evaporation inside tubes: Part II – An updated general flow boiling heat transfer model based on flow pattern. *Int. J. Heat Mass Tran.* 51, 125–135. doi:https://doi.org/10.1016/j.ijheatmasstransfer.2007.04.001.

Cheng, L., Xia, G., Thome, J. R., 2021. Flow boiling heat transfer and two-phase flow phenomena of CO_2 in macro- and micro-channel evaporators: Fundamentals, applications and engineering design. *Appl. Therm. Eng.* 195, 117070. doi:https://doi.org/10.1016/j.applthermaleng.2021.117070.

Clausen, S., Oosterkamp, A., Strøm, K. L., 2012. Depressurization of a 50 km long 24 inches CO_2 pipeline. In: Røkke, N. A., Hägg, M.-B., Mazzetti, M. J. (Eds.), *6th Trondheim Conference on CO_2 Capture, Transport and Storage (TCCS-6)*. BIGCCS / SINTEF / NTNU, Energy Procedia vol. 23, Trondheim, Norway, pp. 256–265. doi:10.1016/j.egypro.2012.06.044.

Collard, A., Apr. 2015. *Blowdown simulation of CO_2 pipelines*. PhD thesis, University College London. URL `https://discovery.ucl.ac.uk/id/eprint/1471446/`.

Collier, J. G., Thome, J. R., 1994. *Convective boiling and condensation*. Oxford University Press, Oxford, UK, third ed. ISBN 0-19-856282-9.

Dittus, F. W., Boelter, L. M. K., 1930. Heat transfer in automobile radiators of the tubular type. *Univ. of California Publ. in Engng.* 2, 443–461.

Drescher, M., Varholm, K., Munkejord, S. T., Hammer, M., Held, R., de Koeijer, G., Oct. 2014. Experiments and modelling of two-phase transient flow during pipeline depressurization of CO_2 with various N_2 compositions. In: Dixon, T., Herzog, H., Twinning, S. (Eds.), *GHGT-12 – 12th International Conference on Greenhouse Gas Control Technologies*. University of Texas at Austin / IEAGHGT, Energy Procedia, vol. 63, Austin, Texas, USA, pp. 2448–2457. doi:10.1016/j.egypro.2014.11.267.

ECCSEL, 2021. Depressurization facility. `https://eccsel.eu/catalogue/facility/?id=113`. Accessed 2023-05-23.

Elshahomi, A., Lu, C., Michal, G., Liu, X., Godbole, A., Venton, P., 2015. Decompression wave speed in CO_2 mixtures: CFD modelling with the GERG-2008 equation of state. *Appl. Energ.* 140, 20–32. doi:10.1016/j.apenergy.2014.11.054.

Fang, X., 2013. A new correlation of flow boiling heat transfer coefficients for carbon dioxide. *Int. J. Heat Mass Tran.* 64, 802–807. doi:10.1016/j.ijheatmasstransfer.2013.05.024.

Fenghour, A., Wakeman, W. A., Vesovic., V., 1998. The viscosity of carbon dioxide. *J. Phys. Chem. Ref. Data* 27(1), 31–44. doi:10.1063/1.556013.

Flechas, T., Laboureur, D. M., Glover, C. J., Aug. 2020. A 2-D CFD model for the decompression of carbon dioxide pipelines using the Peng-Robinson and the Span-Wagner equation of state. *Process Saf. Environ.* 140, 299–313. doi:10.1016/j.psep.2020.04.033.

Friedel, L., Jun. 1979. Improved friction pressure drop correlations for horizontal and vertical two phase pipe flow. In: *Proceedings, European Two Phase Flow Group Meeting*. Ispra, Italy. Paper E2.

Gungor, K. E., Winterton, R. H. S., Mar. 1987. Simplified general correlation for saturated flow boiling and comparisons of correlations with data. *Chem. Eng. Res. Des.* 65 (2), 148–156.

Hammer, M., Deng, H., Austegard, A., Log, A. M., Munkejord, S. T., Nov. 2022. Experiments and modelling of choked flow of CO_2 in orifices and nozzles. *Int. J. Multiphase Flow* 156, 104201. doi:10.1016/j.ijmultiphaseflow.2022.104201.

Hammer, M., Ervik, Å., Munkejord, S. T., 2013. Method using a density-energy state function with a reference equation of state for fluid-dynamics simulation of vapor-liquid-solid carbon dioxide. *Ind. Eng. Chem. Res.* 52 (29), 9965–9978. doi:10.1021/ie303516m.

Hammer, M., Morin, A., Sep. 2014. A method for simulating two-phase pipe flow with real equations of state. *Comput. Fluids* 100, 45–58. doi:10.1016/j.compfluid.2014.04.030.

Hendricks, R. C., Simoneau, R. J., Smith, R. V., Aug. 1970. *Survey of heat transfer to near-critical fluids*. Technical Note TN D-5886, National Aeronautics and Space Administration (NASA), Cleveland, Ohio, USA. URL `https://ntrs.nasa.gov/citations/19710003560`.

IEA, 2020. *Energy Technology Perspectives – Special report on CCUS*. URL `https://www.iea.org/reports/ccus-in-clean-energy-transitions`.

Lei, X., Peng, R., Guo, Z., Li, H., Ali, K., Zhou, X., 2020. Experimental comparison of the heat transfer of carbon dioxide under subcritical and supercritical pressures. *Int. J. Heat Mass Tran.* 152, 119562. doi:https://doi.org/10.1016/j.ijheatmasstransfer.2020.119562.

LeVeque, R. J., 2002. *Finite Volume Methods for Hyperbolic Problems*. Cambridge University Press, Cambridge, UK. ISBN 0-521-00924-3.

Liu, B., Liu, X., Lu, C., Godbole, A., Michal, G., Tieu, A. K., Oct. 2018. A CFD decompression model for CO_2 mixture and the influence of non-equilibrium phase transition. *Appl. Energ.* 227, 516–524. doi:10.1016/j.apenergy.2017.09.016.

Liu, Z., Winterton, R., 1991. A general correlation for saturated and subcooled flow boiling in tubes and annuli, based on a nucleate pool boiling equation. *Int. J. Heat Mass Tran.* 34, 2759–2766. doi:10.1016/0017-9310(91)90234-6.

Log, A. M., Dec. 2023. *Depressurization of CO_2 in pipes: Analysis of experiments and non-equilibrium flashing flow models*. Doctoral thesis, Norwegian University of Science and Technology, Department of Energy and Process Engineering, Trondheim. URL `https://hdl.handle.net/11250/3107027`. ISBN 978-82-326-7553-1.

Log, A. M., Hammer, M., Deng, H., Austegard, A., Hafner, A., Munkejord, S. T., 2023a. Depressurization of CO_2 in pipes: Effect of initial state on non-equilibrium two-phase flow – dataset. Zenodo. doi:10.5281/zenodo.7669536.

Log, A. M., Hammer, M., Deng, H., Austegard, A., Hafner, A., Munkejord, S. T., Jan. 2024a. Depressurization of CO_2 in pipes: Effect of initial state on non-equilibrium two-phase flow. *Int. J. Multiphase Flow* 170, 104624. doi:10.1016/j.ijmultiphaseflow.2023.104624.

Log, A. M., Hammer, M., Munkejord, S. T., 2023b. A flashing flow model for the rapid depressurization of CO_2 in a pipe accounting for bubble nucleation and growth – dataset. Zenodo. doi:10.5281/zenodo.8164913.

Log, A. M., Hammer, M., Munkejord, S. T., 2024b. A flashing flow model for the rapid depressurization of CO_2 in a pipe

accounting for bubble nucleation and growth. *Int. J. Multiphase Flow* 171. doi:10.1016/j.ijmultiphaseflow.2023.104666.

Martynov, S., Zheng, W., Mahgerefteh, H., Brown, S., Hebrard, J., Jamois, D., Proust, C., 2018. Computational and experimental study of solid-phase formation during the decompression of high-pressure CO_2 pipelines. *Ind. Eng. Chem. Res.* 57 (20), 7054–7063. doi:10.1021/acs.iecr.8b00181.

Maxey, W. A., Nov. 1974. Fracture initiation, propagation and arrest. In: *Fifth Symposium on Line Pipe Research*. American Gas Association, Houston, Texas, USA, pp. J1–J31.

Moe, A. M., Dugstad, A., Benrath, D., Jukes, E., Anderson, E., Catalanotti, E., Durusut, E., Neele, F., Grunert, F., Mahgerefteh, H., Gazendam, J., Barnett, J., Hammer, M., Span, R., Brown, S., Munkejord, S. T., Weber, V., Jun. 2020. *A trans-European CO_2 transportation infrastructure for CCUS: Opportunities & challenges*. Report, Zero Emissions Platform, Brussels, Belgium. Available from `https://zeroemissionsplatform.eu/wp-content/uploads/A-Trans-European-CO2-Transportation-Infrastructure-for-CCUS-Opportunities-Challenges.pdf`.

Morin, A., Aug. 2012. *Mathematical modelling and numerical simulation of two-phase multi-component flows of CO_2 mixtures in pipes*. Doctoral thesis, Norwegian University of Science and Technology, Department of Energy and Process Engineering, Trondheim. URL `http://hdl.handle.net/11250/234991`. ISBN 978-82-471-3907-3.

Munkejord, S. T., Austegard, A., Deng, H., Hammer, M., Stang, H. G. J., Løvseth, S. W., Nov. 2020a. Depressurization of CO_2 in a pipe: High-resolution pressure and temperature data and comparison with model predictions. *Energy* 211, 118560. doi:10.1016/j.energy.2020.118560.

Munkejord, S. T., Austegard, A., Deng, H., Hammer, M., Stang, H. G. J., Løvseth, S. W., 2020b. Depressurization of CO_2 in a pipe: High-resolution pressure and temperature data and comparison with model predictions – dataset. Zenodo. doi:10.5281/zenodo.3928227.

Munkejord, S. T., Bernstone, C., Clausen, S., de Koeijer, G., MÃ¸lnvik, M. J., 2013. Combining thermodynamic and fluid flow modelling for CO_2 flow assurance. In: Dixon, T., Yamaji, K. (Eds.), *GHGT-11 – 11th International Conference on Greenhouse Gas Control Technologies*. RITE / IEAGHGT, Energy Procedia, vol. 37, Kyoto, Japan, pp. 2904–2913. doi:10.1016/j.egypro.2013.06.176.

Munkejord, S. T., Deng, H., Austegard, A., Hammer, M., Skarsvåg, H. L., Aasen, A., Jul. 2021. Depressurization of CO_2-N_2 and CO_2-He in a pipe: Experiments and modelling of pressure and temperature dynamics. *Int. J. Greenh. Gas Con.* 109, 103361. doi:10.1016/j.ijggc.2021.103361.

Munkejord, S. T., Hammer, M., Jun. 2015. Depressurization of CO_2-rich mixtures in pipes: Two-phase flow modelling and comparison with experiments. *Int. J. Greenh. Gas Con.* 37, 398–411. doi:10.1016/j.ijggc.2015.03.029.

Munkejord, S. T., Hammer, M., Løvseth, S. W., May 2016. CO_2 transport: Data and models – A review. *Appl. Energ.* 169, 499–523. doi:10.1016/j.apenergy.2016.01.100.

Rathjen, W., Straub, J., 1977. Temperature dependence of surface tension, coexisting curve, and vapor pressure of CO_2, $CClF_3$, $CBrF_3$, and SF_6. In: Hahne, E., Grigull, U. (Eds.), *Heat Transfer in Boiling*, Taylor & Francis Inc., chap. 18. ISBN 0-123-14450-7.

RELAP5, Dec. 2001. *RELAP5/MOD3.3 Code Manual: Volume IV: Models and correlations*. Code Manual NUREG/CR-5535/Rev 1-Vol IV, U.S. Nuclear Regulatory Commission, Washington DC, USA.

RELAP5 Development Team, Dec. 2001. *RELAP5/MOD3.3 Code Manual: Volume I: Code structure, system models, and solution methods*. Code Manual NUREG/CR-5535/Rev 1-Vol I, U.S. Nuclear Regulatory Commission, Washington DC, USA.

Roussanaly, S., Deng, H., Skaugen, G., Gundersen, T., 2021. At what pressure shall CO_2 be transported by ship? An in-depth cost comparison of 7 and 15 barg shipping. *Energies* 14 (18), 271–280. doi:10.3390/en14185635.

Sacconi, A., Mahgerefteh, H., Jan. 2020. Modelling start-up injection of CO_2 into highly-depleted gas fields. *Energy* 191, 116530. doi:10.1016/j.energy.2019.116530.

Samuel, R. J., Mahgerefteh, H., 2019. Investigating the impact of flow rate ramp-up on carbon dioxide start-up injection. *Int. J. Greenh. Gas Con.* 88, 482–490. doi:10.1016/j.ijggc.2019.04.025.

Shah, M., 1982. Chart correlation for saturated boiling heat transfer: Equations and further study. *ASHRAE Trans.* 88 (1), 185–196. URL `https://mmshah.org/publications/oct._2006_HVACRJ.pdf`.

Shah, M. M., Jun. 2006. Evaluation of general correlations for heat transfer during boiling of saturated liquids in tubes and annuli. *HVAC&R Research* 12, 1047–1063. doi:https://doi.org/10.1080/10789669.2006.10391450.

Shukla, P. R., Skea, J., Slade, R., Fradera, R., Pathak, M., Al Khourdajie, A., Belkacemi, M., van Diemen, R., Hasija, A., Lisboa, G., Luz, S., Malley, J., McCollum, D., Some, S., Vyas, P. (Eds.), 2022. *Climate Change 2022: Mitigation of Climate Change. Contribution of Working Group III to the Sixth Assessment Report of the Intergovernmental Panel on Climate Change*. Cambridge University Press, Cambridge, UK and New York, NY, USA. doi:10.1017/9781009157926.

Skarsvåg, H. L., Hammer, M., Munkejord, S. T., Log, A. M., Dumoulin, S., Gruben, G., Mar. 2023. Towards an engineering tool for the prediction of running ductile fractures in CO_2 pipelines. *Process Saf. Environ.* 171, 667–679. doi:10.1016/j.psep.2023.01.054.

Span, R., Wagner, W., Nov.–Dec. 1996. A new equation of state for carbon dioxide covering the fluid region from the triple-point temperature to 1100 K at pressures up to 800 MPa. *J. Phys. Chem. Ref. Data* 25 (6), 1509–1596. doi:10.1063/1.555991.

Spedding, P. L., Hand, N. P., 1997. Prediction in stratified gas-liquid co-current flow in horizontal pipelines. *Int. J. Heat Mass Tran.* 40 (8), 1923–1935. doi:10.1016/S0017-9310(96)00252-9.

Steiner, D., Taborek, J., 1992. Flow boiling heat transfer in vertical tubes correlated by an asymptotic model. *Heat trans. eng.* 13, 43–69. doi:10.1080/01457639208939774.

Stuhmiller, J. H., Dec. 1977. The influence of interfacial pressure forces on the character of two-phase flow model equations. *Int. J. Multiphase Flow* 3 (6), 551–560. doi:10.1016/0301-9322(77)90029-5.

Toro, E. F., Billett, S. J., Nov. 2000. Centred TVD schemes for hyperbolic conservation laws. *IMA J. Numer. Anal.* 20 (1), 47–79. doi:10.1093/imanum/20.1.47.

Vesovic, V., Wakeham, W. A., Olchowy, G. A., Sengers, J. V., Watson, J. T. R., Millat, J., 1990. The transport properties of carbon

dioxide. *J. Phys. Chem. Ref. Data* 19, 763–808. doi:10.1063/1.555875.
Vitali, M., Corvaro, F., Marchetti, B., Terenzi, A., 2022. Thermodynamic challenges for CO_2 pipelines design: A critical review on the effects of impurities, water content, and low temperature. *Int. J. Greenh. Gas Con.* 114, 103605. doi:10.1016/j.ijggc.2022.103605.
Xiao, C., Lu, Z., Yan, L., Yao, S., 2020. Transient behaviour of liquid CO_2 decompression: CFD modelling and effects of initial state parameters. *Int. J. Greenh. Gas Con.* 101, 103154. doi:10.1016/j.ijggc.2020.103154.
Yu, S., Yan, X., He, Y., Chen, L., Hu, Y., Yang, K., Cao, Z., Yu, J., Chen, S., 2024a. Study on the decompression behavior during large-scale pipeline puncture releases of CO_2 with various N_2 compositions: Experiments and mechanism analysis. *Energy* 296, 131180. doi:10.1016/j.energy.2024.131180.
Yu, S., Yan, X., He, Y., Chen, L., Yu, J., Chen, S., 2024b. A new model to predict the small-hole decompression process of long CO_2 pipeline. *Process Saf. Environ.* 187, 443–458. doi:10.1016/j.psep.2024.04.139.
Zheng, W., Mahgerefteh, H., Martynov, S., Brown, S., 2017. Modeling of CO_2 decompression across the triple point. *Ind. Eng. Chem. Res.* 56 (37), 10491–10499. doi:10.1021/acs.iecr.7b02024.

Appendix A. Additional plots for Exp 25

Appendix A.1. Heat-transfer coefficients, HEM

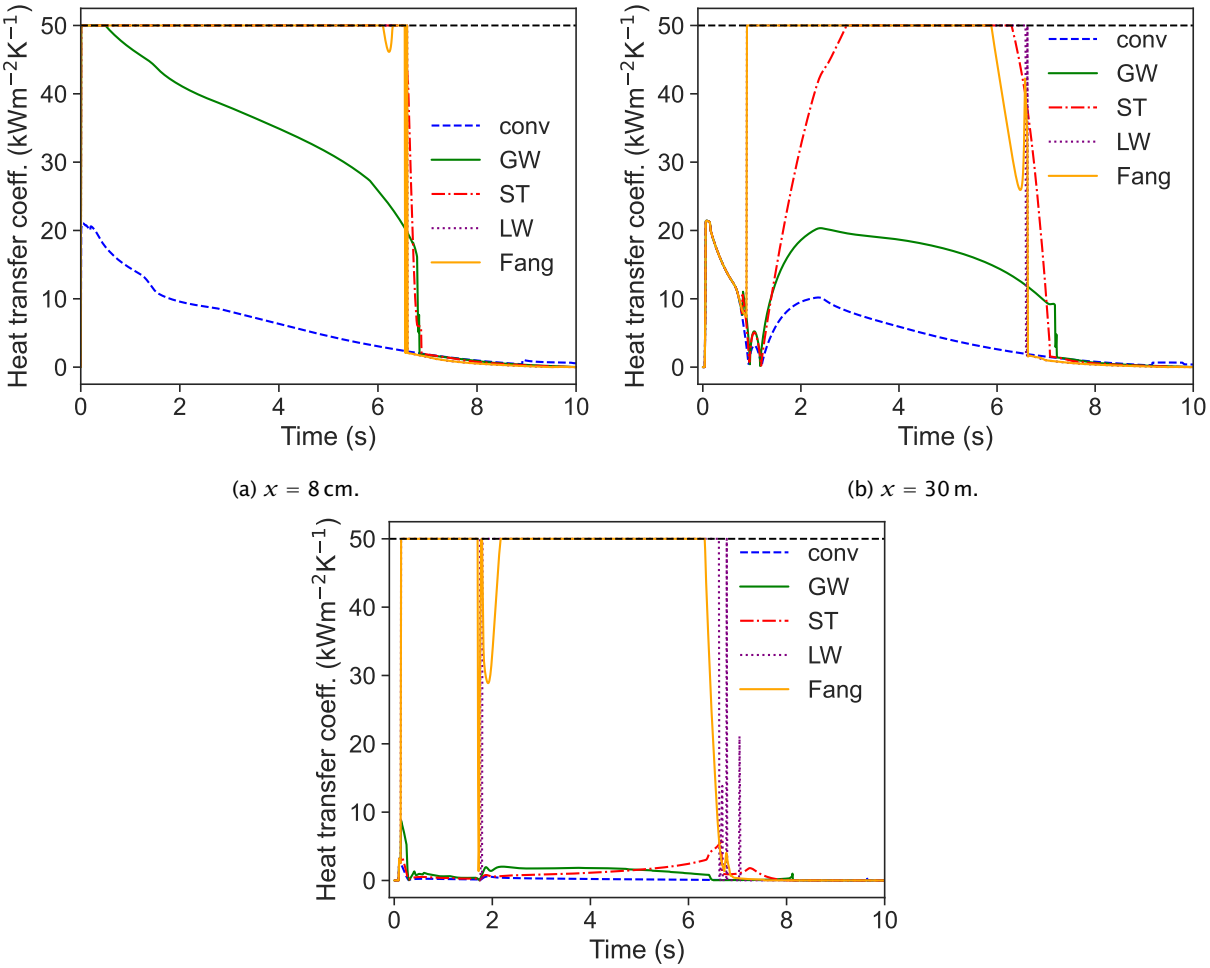

(a) $x = 8$ cm.

(b) $x = 30$ m.

(c) $x = 61$ m.

Figure A.16: Comparison of heat-transfer coefficients predicted by the HEM with different correlations, at different axial positions, for Test 25.

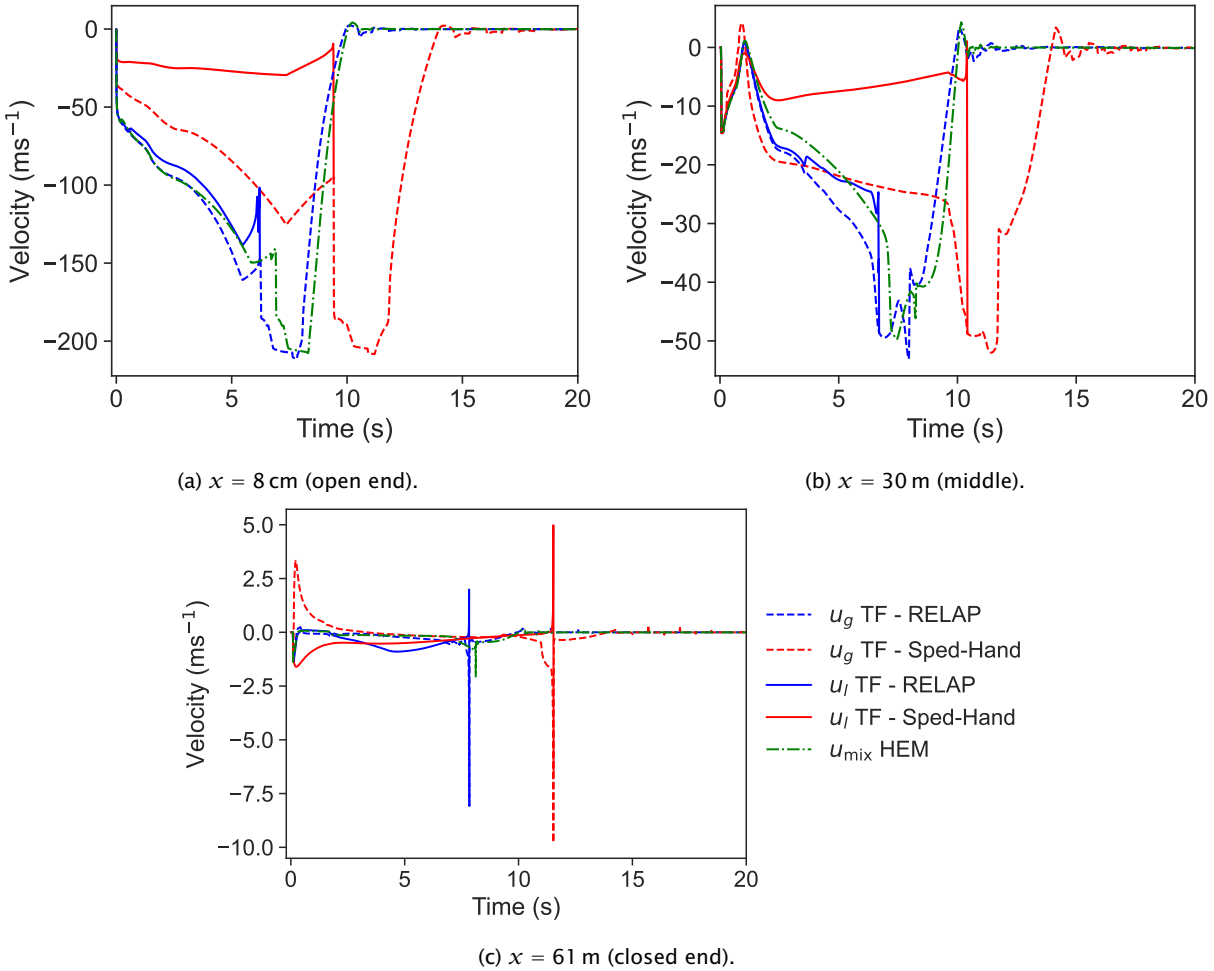

(a) $x = 8$ cm (open end).

(b) $x = 30$ m (middle).

(c) $x = 61$ m (closed end).

Figure A.17: Comparison of flow velocity predicted by the HEM and TFM, at different positions, for Test 25.

Appendix A.3. Pressure predictions, TFM and HEM

In Figure A.18, the predicted pressure evolution of the HEM and that of the TFM for Test 25 are compared to experimental measurements. Once again, the HEM and TFM with flow-regime-based friction models perform fairly similarly. We note that close to the open end (blue), the models have a tendency of underpredicting the pressure by a few bar, up until $t = 6$ s, i.e., before dry-out occurs. After this, the pressure is somewhat overestimated, with the HEM showing the largest deviation from the experimental measurement. On the other hand, the TFM with the Spedding and Hand friction model for stratified flow significantly overpredicts the pressure close to the open end, by around 10 bar. Further inside the pipe, the difference is small between this model and the others for early times. However, for later times, there is also a large overprediction of the pressure, as the liquid is escaping the pipe too slowly, keeping the pressure elevated.

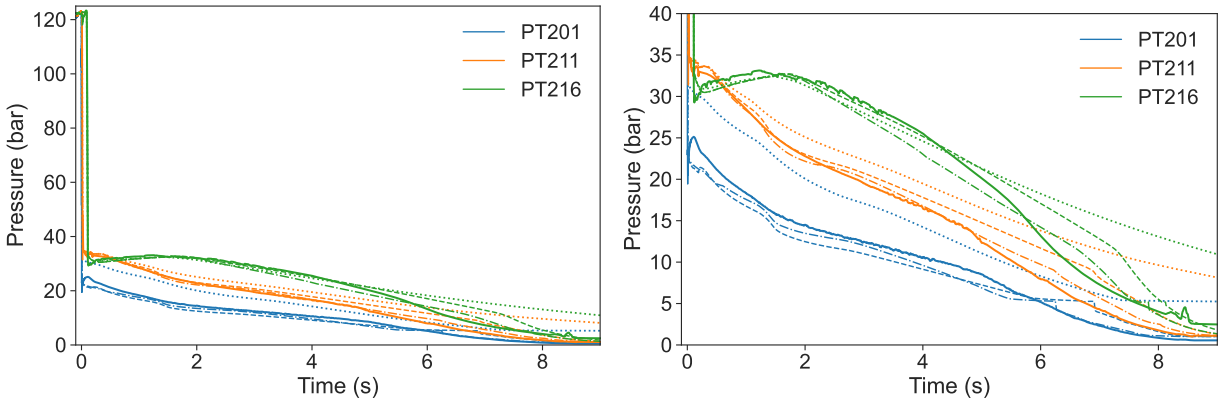

(a) Full pressure evolution

(b) Zoomed in on multiphase flow area

Figure A.18: Comparison of pressure predicted by the HEM (dashed), TFM with RELAP friction (dash-dotted), TFM with Spedding and Hand friction (dotted) and experimental measurements (solid) 8 cm (PT201), 9.6 m (PT211) and 61.5 m (PT216) from the open end of the pipe for Test 25.

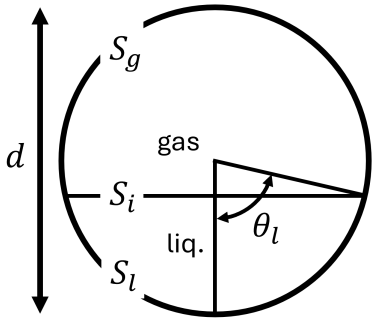

Figure B.19: Illustration of the relevant geometry for stratified flow.

Appendix B. Friction modelling for two-fluid model

In this work, two friction modelling approaches were pursued for the two-fluid model, and they are described in some detail here. These models depend on the topology of the flow. The first model approach assumes stratified two-phase flow, and is described in Appendix B.1. The second model approach is based on a simplified version of the RELAP5 MOD3.3. flow regime map and corresponding friction correlations. This model is briefly described in Appendix B.2.

Appendix B.1. Spedding and Hand: Assumed stratified flow

The Spedding and Hand (1997) friction model assumes stratified, co-current flow. The relevant geometry is shown in Figure B.19. The half wetted angle is estimated based on the explicit approximation of Biberg (1999),

$$\theta_\ell = \pi\alpha_\ell + \frac{3\pi}{2}^{1/3}\left(1 - 2\alpha_\ell + \alpha_\ell^{1/3} - (1.0 - \alpha_\ell)^{1/3}\right). \tag{B.1}$$

The liquid perimeter is then calculated as:

$$S_\ell = \theta_\ell d_{\text{pipe}}, \tag{B.2}$$

the gas perimeter as

$$S_{\text{g}} = (\pi - \theta_\ell) d_{\text{pipe}}, \tag{B.3}$$

and the interface perimeter as

$$S_{\text{i}} = \sin(\theta_\ell) d_{\text{pipe}}. \tag{B.4}$$

The wall frictions and interface friction are:

$$\mathcal{F}_{\text{w}\ell} = f_\ell \frac{\rho_\ell u_\ell |u_\ell|}{2} \frac{S_\ell}{A_{\text{pipe}}}, \tag{B.5}$$

$$\mathcal{F}_{\text{wg}} = f_{\text{g}} \frac{\rho_{\text{g}} u_{\text{g}} |u_{\text{g}}|}{2} \frac{S_{\text{g}}}{A_{\text{pipe}}}, \tag{B.6}$$

and

$$\mathcal{F}_i = f_i \frac{\rho_{\text{g}} (u_{\text{g}} - u_\ell) |u_{\text{g}} - u_\ell|}{2} \frac{S_i}{A_{\text{pipe}}}, \tag{B.7}$$

where f_ℓ is the liquid friction factor, f_{g} is the gas friction factor, f_i is the interface friction factor and A_{pipe} is the cross-sectional area of the pipe.

For the liquid phase, the friction factor is estimated as

$$f_\ell = \begin{cases} \dfrac{24}{Re_\ell}, & \text{if } Re_\ell \le 2100 \\ \dfrac{0.0262}{(\alpha_\ell Re_{\ell,s})^{0.139}}, & \text{if } Re_\ell > 2100, \end{cases} \tag{B.8}$$

where

$$Re_\ell = |u_\ell| \alpha_\ell \rho_\ell \frac{\pi d_{\text{pipe}}}{S_\ell} \frac{d_{\text{pipe}}}{\nu_\ell} \tag{B.9}$$

and

$$Re_{\ell,s} = |u_\ell| \alpha_\ell \rho_\ell \frac{d_{\text{pipe}}}{\nu_\ell}. \tag{B.10}$$

The gas phase friction factor is estimated as

$$f_{\text{g}} = \begin{cases} \dfrac{16}{Re_{\text{g}}}, & \text{if } Re_{\text{g}} \le 2100 \\ \dfrac{0.046}{Re_g^{0.2}}, & \text{if } Re_{\text{g}} > 2100, \end{cases} \tag{B.11}$$

where

$$Re_{\text{g}} = |u_{\text{g}}| \alpha_{\text{g}} \rho_{\text{g}} \frac{\pi d_{\text{pipe}}}{S_{\text{g}} + S_{\text{if}}} \frac{d_{\text{pipe}}}{\nu_{\text{g}}}. \tag{B.12}$$

Finally, the interface friction factor is estimated as

$$f_{\text{i}} = f_{\text{g}}(\alpha_{\text{g}} = 1.0) \left(1.76 \frac{\alpha_{\text{g}} |u_{\text{g}}|}{6} + k \right), \tag{B.13}$$

where

$$k = 2.7847 \log_{10} \left(\frac{\alpha_\ell |u_\ell|}{\alpha_\ell |u_\ell| + 6} \right) + 7.8035. \tag{B.14}$$

Note that the interface friction factor can become negative for certain cases where one of the phases is dominating the flow. If this happens, we limit the interface friction factor to zero to avoid an unphysical result.

Appendix B.2. Simplified RELAP flow regime map

The complete RELAP flow regime map has a number of details which are not included here for the sake of brevity. For the full details, the reader is referred to the RELAP5/MOD3 manual. However, the main features and differences between our model and the RELAP one are provided here.

The simplified flow regime map used in the present work is shown in Figure B.20. The main difference between the RELAP5 MOD3.3 flow regime map is that slug flow is ignored, and treated simply as a transition from bubbly to annular mist flow. We further assume a high mass flux and take

$$\alpha_{\text{BS}} = 0.5, \tag{B.15}$$

as opposed to $\alpha_{\text{BS}} = 0.25$ which is set in RELAP for lower mass fluxes. We further have

$$\alpha_{\text{SA}} = 0.8, \ \alpha_{\text{AM}} = 0.9999. \tag{B.16}$$

Finally,

$$u_{\text{crit}} = \frac{1}{2} \left(\frac{(\rho_\ell - \rho_{\text{g}}) g \alpha_{\text{g}} A}{\rho_{\text{g}} d \sin(\theta_{\text{g}})} \right)^{\frac{1}{2}} \left(1 - \cos(\theta_{\text{g}}) \right), \tag{B.17}$$

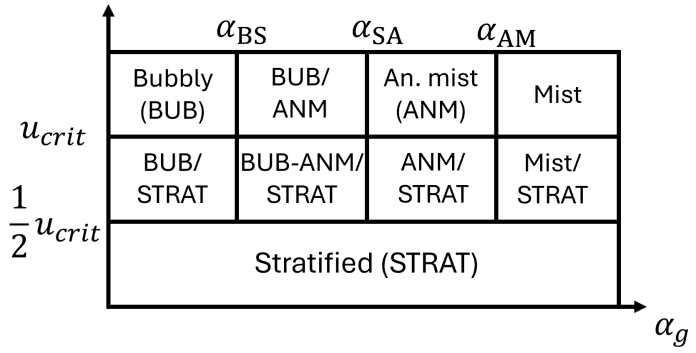

Figure B.20: The simplified flow regime map based on RELAP5 MOD3.3.

where θ_g is the half dry angle, $\theta_g = \pi - \theta_\ell$ and θ_ℓ is calculated using Equation (B.1). Each flow regime has its own friction correlations that are used to determine the wall frictions $\mathcal{F}_{w\ell}, \mathcal{F}_{w,g}$ and the interface friction $\mathcal{F}_i$. The non-transition flow regimes are calculated exactly as specified in the RELAP5 MOD3.3. manual. The transition flow regimes are calculated using interpolation between the flow regime frictions at the boundaries of the transition regime.

For our simplified flow model, we have a transition directly from bubbly to annular-mist flow. We employ a simple linear interpolation between these two regimes to obtain the related frictions. Similarly to RELAP, we also have the transition from stratified to non-stratified flows. For these transitions, we average the frictions with the dispersion-degree $0 < \delta < 1$ of the flow:

$$\mathcal{F}_\xi = \delta^5 \mathcal{F}_\xi^{\text{DISP}} + (1 - \delta^5)\mathcal{F}_\xi^{\text{STRAT}}, \tag{B.18}$$

where $\xi \in wg, wl, i$, and DISP denotes any of the dispersed flow regimes (bubbly, bubbly-annular-mist, annular-mist and mist) and

$$\delta = \frac{|u_\ell - u_g| - \frac{1}{2}u_{\text{crit}}}{u_{\text{crit}} - \frac{1}{2}u_{\text{crit}}}. \tag{B.19}$$

Here, the non-linear interpolation is applied to avoid a too sudden change in friction when transitioning from dispersed to stratified flow.